JHI Journal of Human Immunity

ARTICLE

Oncostatin M receptor deficiency as a novel candidate genetic cause of autosomal recessive hyper-IgE syndrome

Sisse Andersen[1*], Kristian Assing[2*], Julie Jensen[1], Line Dahlerup Rasmussen[3], Christian B. Laursen[4], Christoffer D. Dellgren[5], Daniëla Maria Hinke[1], Søren E. Degn[1], and Trine H. Mogensen[1,6]

Hyper-IgE syndrome (HIES) is characterized by elevated serum IgE levels, eczema, and recurrent skin and pulmonary infections, classically caused by autosomal dominant (AD) STAT3 loss-of-function variants. Here we describe a patient presenting with elevated IgE levels, atopic eczema, chronic pulmonary aspergillosis, and bone fractures, homozygous for a rare missense variant in the oncostatin M receptor (*OSMR*) gene. We demonstrate that the patient OSMR V436D variant is deleterious and leads to decreased OSMR surface expression and impaired OSM-induced STAT3 phosphorylation. Blood profiling showed elevated IgE-expressing plasmablasts and peripheral T follicular helper cells and atypical memory B cells. A germinal center model revealed a B cell–extrinsic defect in concordance with a largely fibroblast-confined phenotype. Finally, reconstitution of patient fibroblasts led to functional complementation of the cellular phenotype. We propose OSMR deficiency as a novel genetic etiology of AR-HIES, resembling the clinical and immunological phenotype of STAT3 AD-HIES, but mediating its phenotypic profile mainly in the stromal rather than hematopoietic compartment.

Introduction

Hyper-immunoglobulin E syndrome (HIES), originally termed Job's syndrome, is a collection of rare inborn errors of immunity (IEI) characterized by the clinical triad of elevated IgE serum levels, eczema, and recurrent skin and pulmonary infections (1, 2, 3). Characteristic disease presentations of Job's syndrome consist of recurrent "cold" staphylococcal skin abscesses, pulmonary staphylococcal and *Aspergillus* infections, chronic mucocutaneous candidiasis (CMC), eosinophilia, as well as a somatic/extra-hematopoietic phenotype, including facial, skeletal, and dental abnormalities, such as craniosynostosis, osteopenia, and scoliosis, and as more recently reported cranial artery aneurisms (1, 4, 5). Disease-causing monoallelic dominant-negative (DN) missense variants of the gene encoding signal transducer and activator of transcription 3 (STAT3) were first reported in 2007 (6, 7, 8, 9, 10), and subsequently many more patients with AD-HIES due to DN STAT3 variants have been reported (6, 7, 8, 9, 10, 11).

Beyond the originally described STAT3 autosomal dominant (AD)-HIES, several other genetic etiologies of AD- or autosomal recessive (AR)-HIES with very similar and overlapping, yet not identical, clinical presentations have been described, prompting the notion of a collection of hyper-IgE syndromes (8, 11, 12, 13, 14). For AD-HIES, these include mutations in the receptor subunit glycoprotein 130 (gp130) encoded by *IL6ST* (15), loss-of-function (LOF) mutations in *CARD11* (16), and AD gain-of-function (GOF) mutations in *STAT6* (17). Moreover, two molecules involved in the TGFβ pathway, inherited as GOF mutations in TGFβ receptor complex (*TGFBR1/2*) (Louys-Dietz syndrome) or LOF mutations in *ERBIN*, also cause AD-HIES (18, 19). In addition, HIES inherited in an AR manner can be caused by biallelic mutations in a number of different genes, including *DOCK8* (20), the STAT3-inducing transcription factor *ZNF341* (21, 22), the phosphoglucomutase *PGM3* (23, 24), through defect glycosylation of the receptor subunit GP130 (25), *SPINK5* (26), biallelic LOF variants in *IL6ST/GP130* (27) (also a cause of AD-HIES in monoallelic form), and biallelic mutations in *IL6R* encoding the IL-6 receptor (28).

STAT3 is broadly expressed in many tissues and acts downstream of numerous important cytokine receptors, including IFNAR1, IL-6R, IL-10R, IL-11R, IL-21R, IL-22R, IL-23R, oncostatin M (OSM) receptor (OSMR) and leukemia inhibitory factor receptor (LIFR) (29), thereby accounting for the heterogenous

---

[1]Department of Biomedicine, Aarhus University, Aarhus, Denmark; [2]Department of Clinical Immunology, Odense University Hospital, Odense, Denmark; [3]Department of Infectious Diseases, Odense University Hospital, Odense, Denmark; [4]Department of Pulmonology, Odense University Hospital, Odense, Denmark; [5]Department of Clinical genetics, Odense University Hospital, Odense, Denmark; [6]Department of Infectious Diseases, Aarhus University Hospital, Aarhus, Denmark.

*S. Andersen and K. Assing contributed equally to this paper. Correspondence to Trine H. Mogensen: trine.mogensen@biomed.au.dk.

Rockefeller University Press https://doi.org/10.70962/jhi.20250119

presentation and complexity of diseases caused by abnormal STAT3 activity. Given the central position and key role of this transcription factor, defects in STAT3 or STAT3-inducing cytokine receptors result in dysregulated signaling pathways, which in turn inhibit the generation of T helper 17 (Th17) cells and neutrophil chemotaxis, resulting in abnormal immune responses and insufficient protection against bacterial and fungal infections (29). Moreover, defective STAT3 signaling leads to a shift toward Th2-dominated responses (30), promoting elevated IgE production and eosinophilia, which account for the elevated IgE levels and atopic features, such as eczema and asthma.

The *OSMR* gene (5p13.1) encodes the OSMR and is a membrane-embedded receptor belonging to the family of type I cytokine receptors (31). OSMR is a constituent of two surface receptor complexes, as it heterodimerizes with gp130 to form a receptor for OSM and with interleukin 31RA (IL31RA) to form a receptor for IL-31 (32). OSM-induced OSMR-mediated signaling mediates pleiotropic effects on inflammation, tissue remodeling, hematopoiesis, cell differentiation, and cancer (33). IL-31–induced OSMR-mediated signaling shares similarities with OSM-OSMR signaling but is more specific to cutaneous inflammation, T cell differentiation, and allergic diseases (34). Structurally, OSMR highly consists of three major domains. The extracellular domain is crucial for the interaction of OSMR with functionally related membrane proteins, such as gp130 or IL31RA, and this domain comprises four tandemly arranged, highly conserved, subdomains termed type III fibronectin (FNIII) domains (31). Following the extracellular domain is the short transmembrane domain, which culminates in the C-terminal cytoplasmic domain, the latter being responsible for OSMR downstream signaling (35). Upon cytokine activation, Janus-associated kinases phosphorylate tyrosine residues in the cytoplasmic domain of these receptors leading to the recruitment and activation of STAT1, STAT3, and, to a lesser extent, STAT5 (36, 37, 38, 39).

OSM belongs to the IL-6 family cytokines, including IL-6, IL-11, IL-27, LIF, OSM, IL-35, cardiotrophin-1, and ciliary neurotrophic factor (40). In addition to OSMR/gp130, OSM also binds to a receptor complex constituted by gp130 and the LIFR, although with lower affinity (41). Both gp130 and LIFR contain cytoplasmic domains capable of signal transduction, but LIFR tissue expression is much more restricted than OSMR tissue expression, as the LIFR is only expressed at low levels in adult epithelial, mesenchymal, and hematopoietic cells. The LIFR therefore likely fulfills its primary physiological role during embryogenesis (42). IL-31 signals exclusively through the OSMR/IL-31RA receptor complex. The effects of IL-31 are diverse but primarily documented in vitro and involve leukocytes, keratinocytes, airway, and intestinal epithelial cells as well as neurons (34). However, some evidence suggests that IL-31 plays important roles in airway, skin, and intestinal inflammation in humans (43, 44).

According to the Online Mendelian Inheritance in Man database, heterozygosity for *OSMR* variants is associated with familial primary localized cutaneous amyloidosis (FPLCA), an AD disease characterized by itchy, thickened, red skin with amyloid deposits in the superficial dermis, the skin being the sole organ affected in this disorder (45, 46, 47). No other clearly defined disease entities have hitherto been associated with OSMR variants. Recently, however, a homozygous variant in OSM, observed in a consanguineous family, has been associated with inherited severe bone marrow failure syndrome evidenced by profound anemia, thrombocytopenia, and neutropenia but without susceptibility to infection. Functionally, this OSM variant affects the C-terminal part of OSM, which is important for interaction with the OSMR (48). Finally, defects in LIFR-gp130 cause Stüve-Wiedemann syndrome, defined by profound bone abnormalities, respiratory distress, and autonomous nervous system anomalies with early lethality (13).

Collectively, the genetic, immunological, and clinical infectious and extra-hematopoietic spectrum of HIES, some of which have been reclassified into combined immunodeficiencies, display a heterogenous picture (12, 49). Here we sought to investigate a new genetic etiology of AR-HIES in a patient with OSMR deficiency to obtain further insights into the pathogenesis of this disorder and to improve diagnosis of patients with clinical HIES in whom none of the currently established gene defects can be identified.

Results

Clinical history of a 57-year-old male patient with eczema, asthma, skin infections, and chronic cavitary pulmonary aspergillosis

We investigated a 57-year-old man of Caucasian (Danish) descent with a clinical history of severe atopic dermatitis, eczema, and asthma throughout life. He experienced slow wound healing and frequent secondary staphylococcal skin infections and pustules, but only seldom skin abscesses. Dental status was poor with tooth retraction at a young age and a previous history of tooth abscesses (Fig. 1 A). From the age of 20 years, he experienced one or more bacterial pneumonias per year, as well as episodes of oral candidiasis but not CMC nor invasive candida infection. At the age of 45 years, he had a distal radial fracture in response to a low energy trauma, a subsequent bone density scan showing osteopenia, originally presumed to be related to prolonged steroid therapy for his asthma. Due to prolonged coughing, dyspnea, and chest pain, he was referred to evaluation, and computed tomography of the chest showed signs of chronic pulmonary aspergillosis with a thick-walled cavity in the left upper lobe characteristic of an aspergilloma (Fig. 1 B). Bronchoscopy revealed *Aspergillus fumigatus* DNA and a positive *Aspergillus* galactomannan antigen (AGA) test. Blood tests at that time showed increased *Aspergillus* IgG (IgG; 157 mg/L, normal range <26.9 mg/L) and IgE (37,900 IU/L, normal range <350 IU/L), slightly increased eosinophil count (0.66×10^9/L, normal range $<0.5 \times 10^9$/L), and a very high IgE (IgE: $34{,}000 \times 10^3$ IU/L, normal range <100 IU/L) (Table S1). A diagnosis of chronic cavitary pulmonary aspergillosis (CCPA) was established, and the patient was treated with long-term antifungal itraconazole and also started on prophylactic sulfamethoxazole and trimethoprim (Bactrim) prophylaxis. A skin biopsy showed perivascular inflammation with lymphocytes and eosinophils but no amyloid deposits.

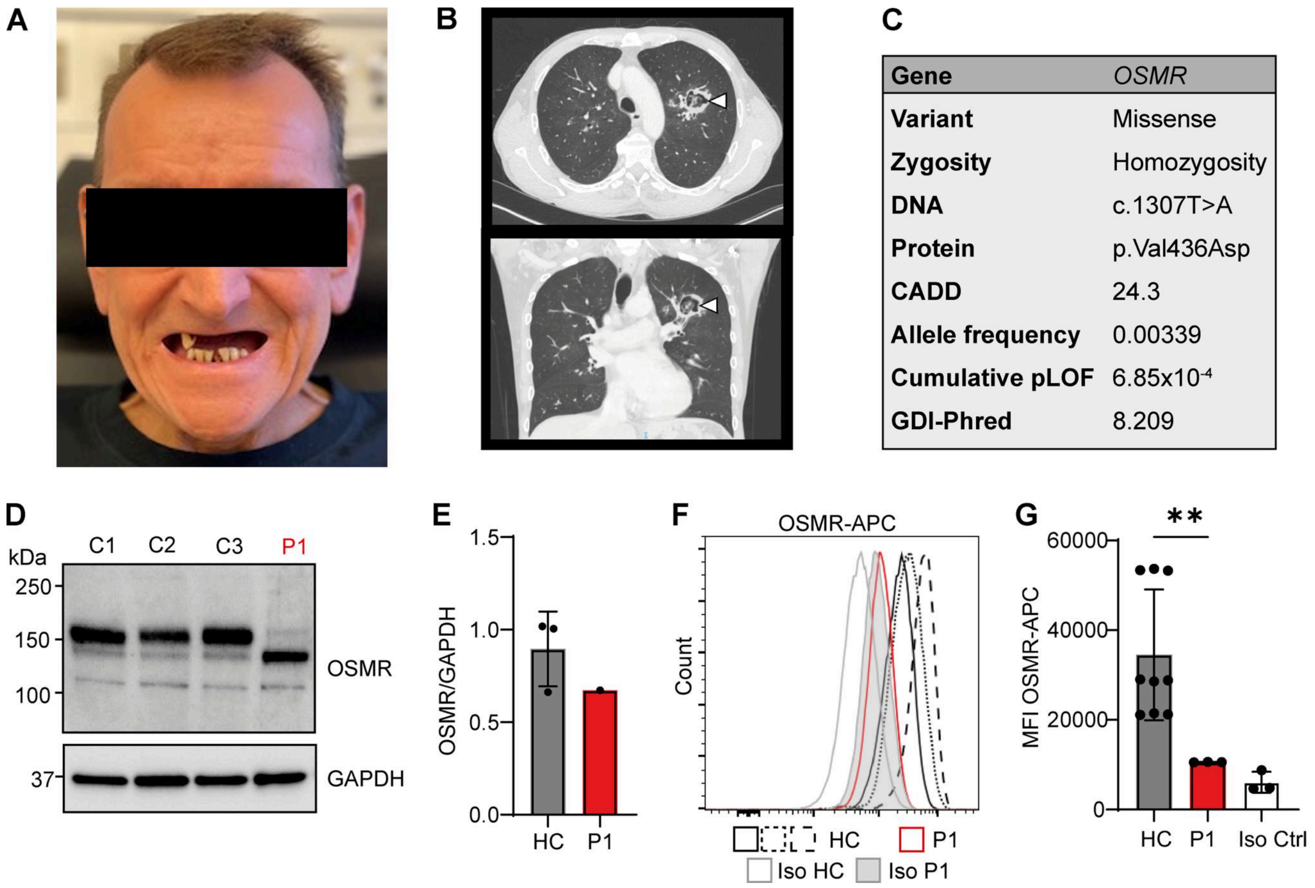
[redacted]

Gene	*OSMR*
Variant	Missense
Zygosity	Homozygosity
DNA	c.1307T>A
Protein	p.Val436Asp
CADD	24.3
Allele frequency	0.00339
Cumulative pLOF	6.85×10^{-4}
GDI-Phred	8.209

Figure 1. **Identification of biallelic *OSMR* variants in a patient with HIES. (A)** Characteristic facies with coarse features and poor dentition. **(B)** Computed tomography of the chest with findings consistent with CCPA. A single pulmonary cavity (arrowheads) containing a "fungal ball" is present in the right upper lobe: the transverse picture is seen from below and the X ray is looking at the patient from the front, ie inverted right/left. Upper part: Axial view. Bottom part: Coronal view. **(C)** Table with genetic information on the *OSMR* variant identified in P1. **(D and E)** Immunoblot of OSMR in NHDFs from healthy controls (HCs) and patient (P1), bands were quantified by ImageJ (E). **(F and G)** FC of surface expressed OSMR in NHDFs from three healthy controls (HCs) and patient (P1) (F) with the mean of fluorescence intensities (MFI) plotted (G). Similar results from western blot and FC have been observed twice prior. Statistics were calculated using the unpaired *t* test. ** = P < 0.01. Source data are available for this figure: SourceData F1.

Clinical immunological evaluation and immune phenotyping

Based on the highly elevated IgE over time (Fig. S1 A) and increased occurrence of infections, the patient was referred to the Department of Infectious Diseases for evaluation of suspected HIES. Standard immunological screening revealed normal serum concentrations of IgA, IgM, and IgG (Table S1). Serum IgE was markedly elevated to levels ranging from 18,200 to 34,000 IU/ml and with mild eosinophilia and slight anemia in the range between 6.8 and 7.8 mmol/L (normal range 8.3–10.5 mmol/L) (Fig. S1 and Table S1). Peripheral $CD19^+$, $CD4^+$, and $CD8^+$ lymphocyte concentrations were normal (Table S1), but patient $CD4^+$ T cells displayed an activated ($HLA\text{-}DR^+$: 30%) phenotype (Table S1). Lymphocyte subset analysis showed normal distributions of Th2, Th9, and Th17 subsets, except for slightly elevated peripheral follicular helper T (pTFH) cell ($CD4^+$ $CXCR5^+$ $PD1^+$ $ICOS^+$) frequencies in the patient (Table S1 and Fig. S2). Serum levels of IL-4 and IFNγ were likewise within normal ranges. Patient $CD8^+$ T cells showed a reduced proliferation index and a diminished responding fraction (Table S1). Stimulated patient $CD4^+$ T cells displayed no relative expansion of Th17 cells ($CD4^+$ $IL\text{-}17A^+$ T cells) nor Th2 cells ($CD4^+$ $IL\text{-}4R\alpha^+$ T cells) compared to those of controls (Fig. S3).

Identification of a novel p.Val436Asp (V436D) missense variant in OSMR in the patient

Since HIES was suspected based on the clinical presentation and paraclinical findings as well as a HIES score of >20 (Fig. S1 B), whole-genome sequencing (WGS) was performed, revealing that P1 was homozygous for a missense variant (c.1307T > A) in the gene (*OSMR*) coding for the OSMR, in which valine was substituted for aspartic acid at amino acid position 436 (Val436Asp, V436D) (Fig. 1 C). The *OSMR* variant has a combined annotation-dependent depletion (CADD) score of 24.3 (with a mutation significance cutoff [MSC] = 19.3) and a minor allele frequency (MAF) of 3.39×10^{-3}. Immunoblotting of whole-cell lysates from P1 fibroblasts revealed that endogenous OSMR is expressed at a slightly reduced level and migrating further in the gel, reflecting a reduced molecular weight of the OSMR protein (Fig. 1, D and E). A significant reduction in OSMR surface expression on patient dermal fibroblasts compared to controls was found by flow cytometry (FC) (Fig. 1, F and G). The genome was also searched for known or predicted pathogenic variants in classified IEI genes, particularly those previously associated with AD- or AR-HIES, none of which were identified (50). Of note, the patient was found to be heterozygous for missense variants in ZNF341 and DOCK8 (Table S2), etiologies of HIES if present in homozygosity. However, the CADD score of the ZNF341 variant is below MSC and therefore considered unlikely to have any deleterious effects. Although the DOCK8 variant has a CADD score above the MSC, in the context of a high GDI-Phred index, DOCK8 is a highly mutated gene, also strongly arguing against a functional role of this variant.

Functional evaluation of STAT3 phosphorylation by predicted deleterious *OSMR* variants in the general population

All homozygous *OSMR* variants reported in gnomAD v4.1 were plotted with CADD-MAF pViz plot, showing 11 homozygous *OSMR* variants with a CADD score >20 and above the MSC and less frequent than 0.1 (Fig. 2 A). The MAF varies among these 11 variants from very frequent 2.54×10^{-2} (G587D) to very rare 3.72×10^{-6} (G927E), with the patient variant appearing at a MAF of 3.39×10^{-3}, and as depicted, the variants are localized in different domains of the OSMR molecule (Fig. 2 B). Therefore, it was important to clarify whether the *OSMR* variant identified in P1 is functionally deleterious and verify that this is not the case for the remaining predicted deleterious variants in the general healthy population. The majority of these 11 OSMR variants are localized in the FNIII domains of the extracellular domain of the OSMR molecule, as is also the case for the *OSMR* variant identified in P1, and consistent with the position of other disease-causing variants in general within the *OSMR* gene (46, 51). The amino acid substitution in the OSMR variant of P1 is located in the beginning of the second of the four FNIII domains of OSMR (31).

To functionally study the *OSMR* variants in a biochemical assay on an isogenic background, we generated HEK293 cells deficient in both OSMR and LIFR to impair the OSM signaling. Two single-cell clones (SCCs) with OSMR_LIFR double KO were generated by CRISPR/Cas9 technology (Fig. 2 C), and functional studies showed that both clones were impaired in phosphorylation of STAT3 in response to OSM stimulation, while STAT3 phosphorylation was similar downstream of OSMR WT and OSMR P1 variant downstream of IL-6 stimulation (Fig. 2, D and E). IL-11 stimulation activated STAT3 to a lesser extent than OSM and IL-6, so it was difficult to conclude whether this downstream signaling was compromised. With this functional validation of the OSMR_LIFR double KO SCCs, it was safe to continue with overexpression of OSMR WT and the different variants followed by OSM stimulation to examine for STAT3 phosphorylation as a functional measure of OSMR signaling capacity (Fig. 2, F and G). These data showed that the P1 OSMR variant was markedly impaired in phosphorylation of STAT3 almost at the same level as transfection control (GFP) and in strong contrast to the robust STAT3 phosphorylation observed in SCCs expressing OSMR WT. Importantly, the other 10 *OSMR* variants reported in gnomAD all showed STAT3 phosphorylation comparable to OSMR WT in response to OSM stimulation, demonstrating intact signaling and no functional defect. Based on this, we conclude that the biallelic *OSMR* variant harbored by P1 is functionally defective, unlike the other *OSMR* variants with CADD score >20. Interestingly, when expressing the different *OSMR* variants, two differentially migrating bands were consistently observed. Notably, the V436D variant was the only variant that did not appear to have an upper band >150 kDa, which was the most prominent band for OSMR WT and most variants. The OSMR C687G variant appeared to have very little upper OSMR band, but no defect was observed with regards to STAT3 phosphorylation after OSM stimulation (Fig. 2 F). Finally, N-deglycosylase PNGase treatment of cell lysates showed that the upper OSMR bands of the many OSMR variants seen on western blotting (WB) represent N-linked glycosylated OSMR forms, since these upper bands disappeared after PNGase treatment, thereby indicating that the patient *OSMR* variant is defective in N-glycosylation (Fig. S3 C).

Since OSMR can cooperate with other receptor subunits of the IL-6 superfamily, we also tested responses to other IL-6 superfamily cytokines. We found that the OSMR variant from P1 impacted on the OSM signaling pathway exclusively, since signaling in response to IL-6 and IL-11 were both similar between OSMR WT and variant (Fig. 2, H and I). Since HEK293 cells do not express the α receptor subunit of the IL-31 receptor (IL31RA), which forms a receptor complex with OSMR, no STAT3 phosphorylation was detectable after IL-31 stimulation, although an effect of OSMR variant compared to OSMR WT here cannot be excluded.

Patient fibroblasts show abnormal OSMR glycosylation pattern and impaired OSM-induced signaling via the OSM/gp130 receptor complex

Although OSMR harbors 13 N-linked glycosylation sites and one O-linked glycosylation site, none of these glycosylation sites include residue 436. To examine further the effect of the variant on OSMR protein expression, we performed immunoblotting on cell extracts from P1 and healthy controls treated with the N-deglycosylase PNGase F. This treatment resulted in the WT OSMR protein migrating further in the gel close to the gel position for OSMR V436D, whereas the OSMR V436D variant almost completely disappeared, suggesting deficient N-glycosylation of the OSMR variant and impaired N-glycosylation possibly underlying the increased destabilization of the OSMR variant protein (Fig. 3, A and B), in accordance with the results of expression of PNGase-treated OSMR variants in the HEK293 model system (Fig. S3 C). Treatment of fibroblasts with the protein synthesis inhibitor cycloheximide, however, showed similar degradation kinetics between OSMR V436D and OSMR WT, thereby suggesting N-glycosylation as a key determinant for the very low expression of the OSMR V436D variant rather than accelerated degradation (Fig. 3, C and D).

Next, we investigated signaling downstream of OSM stimulation. Whereas OSM stimulation of fibroblasts from controls induced strong phosphorylation of STAT3 and STAT5, this signal was almost completely abolished in patient fibroblasts, as well as more moderately reduced phosphorylation of ERK1/2 in patient compared to healthy controls (Fig. 3, E and F). The defective STAT3 phosphorylation in patient fibroblast harboring OSMR V436D was exclusive to the OSMR/gp130 receptor complex, since IL-6 and IL-11 stimulation resulted in marked and

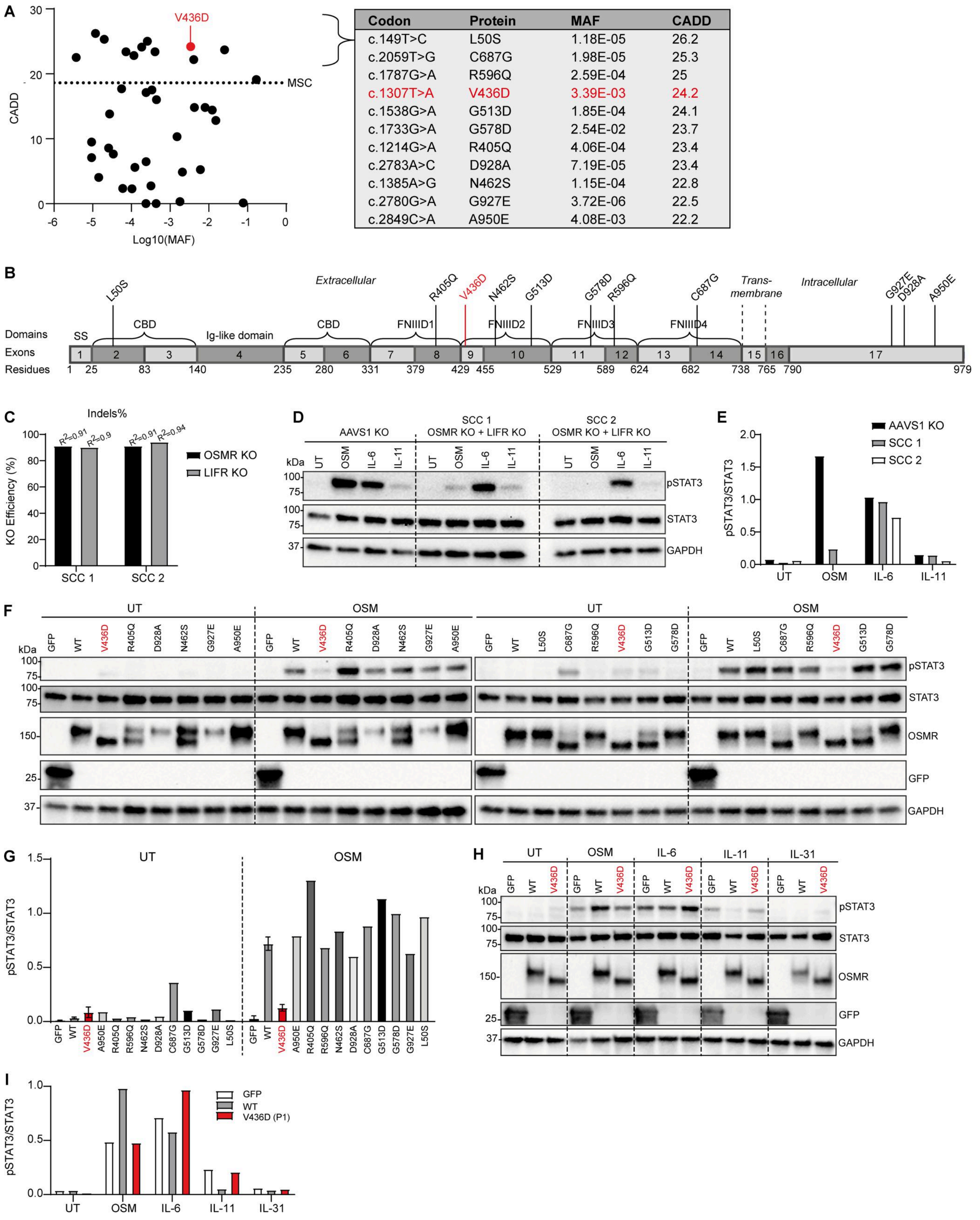

Codon	Protein	MAF	CADD
c.149T>C	L50S	1.18E-05	26.2
c.2059T>G	C687G	1.98E-05	25.3
c.1787G>A	R596Q	2.59E-04	25
c.1307T>A	V436D	3.39E-03	24.2
c.1538G>A	G513D	1.85E-04	24.1
c.1733G>A	G578D	2.54E-02	23.7
c.1214G>A	R405Q	4.06E-04	23.4
c.2783A>C	D928A	7.19E-05	23.4
c.1385A>G	N462S	1.15E-04	22.8
c.2780G>A	G927E	3.72E-06	22.5
c.2849C>A	A950E	4.08E-03	22.2

Figure 2. **Functional evaluation of predicted potentially deleterious homozygous missense *OSMR* variants from the general population (overexpressed in OSMR- and LIFR-deficient HEK293T cells). (A)** All homozygous *OSMR* variants from gnomAD v4.1 plotted as CADD score versus MAF. The red dot refers to the variant of P1. Dotted line represents the MSC (>19.3) with 95% confidence interval. A total of 11 homozygous missense *OSMR* variants predicted to be potentially deleterious (CADD score >20) from gnomAD v4.1 are listed in the table with the variant identified in P1 shown in red. **(B)** Localization of the

predicted deleterious *OSMR* variants in different domains of the OSMR protein with the variant in P1 shown in red. CBD, cytokine binding domain. **(C)** The surface receptors OSMR and LIFR known to bind OSM were knocked out in HEK293 cells by the CRISPR/Cas9 technique. KO efficiencies of two SCCs were determined by EditCo's ICE Analysis Tool (52) and shown as indels. **(D and E)** Functional validation of nucleofected HEK293T cells with CRISPR guides targeting AAVS1 (control) or OSMR and LIFR from C. Cells were stimulated for 30 min by either OSM (50 ng/ml), IL-6 (100 ng/ml), or IL-11 (100 ng/ml) prior to harvest of whole-cell lysates for WB for the visualization of pSTAT3, STAT3, and GAPDH and quantification of WB band intensities shown in E. **(F and G)** OSMR-LIFR double KO HEK293 cells (SCC 2) overexpressing GFP, OSMR WT, or various OSMR variants from gnomAD by transfection. Cells were left untreated (UT) or stimulated with 50 ng/ml OSM for 30 min prior to harvest of whole-cell lysates for WB for the visualization of pSTAT3, STAT3, OSMR, GFP, and GAPDH, with quantification of WB band intensities shown in G. **(H and I)** OSMR-LIFR double KO HEK293 cells (SCC 2) overexpressing GFP, OSMR WT, or the OSMR P1 variant V436D by transfection. Cells were left untreated (UT) or stimulated with OSM (50 ng/ml), IL-6 (100 ng/ml), IL-11 (100 ng/ml), or IL-31 (100 ng/ml) for 30 min prior to harvest of whole-cell lysates for WB for the visualization of pSTAT3, STAT3, and GAPDH and quantification of WB band intensities shown in I. Source data are available for this figure: SourceData F2.

comparable phosphorylation levels of STAT3 between P1 and controls in fibroblasts (Fig. 3, G–J), demonstrating the integrity of STAT3 phosphorylation in response to other stimuli than those binding to OSMR. In addition to gp130, OSMR can also form a heterodimer with IL31RA, thereby creating a receptor complex for IL-31. As observed in HEK293 cells, no STAT3 activation was observed after IL-31 stimulation (Fig. 3, G and H), which may be due to IL31RA surface expression being very low compared to OSMR (32, 53). Functionally, OSM-induced STAT3 and ERK1/ERK2-dependent gene expression was compromised, since expression levels of *IL-6*, *IRF7*, *CXCL10*, and *ICAM1* after 6-h OSM stimulation were reduced in P1 fibroblasts compared to those of controls, reaching statistical significance for IL-6 and CXCL10 (Fig. 3 K).

Evaluation of constitutive and induced expression and signaling of OSMR in PBMC populations

Similar to the observations in fibroblasts, OSM-induced STAT3 phosphorylation was reduced in patient peripheral blood mononuclear cells (PBMC)s (Fig. 4, A and B). However, OSM only activated STAT3 when using high concentrations (100 ng/ml of OSM which is 20-fold more than the 5 ng/ml used for fibroblasts), reflecting less OSMR surface expression on PBMCs as compared to fibroblasts. Accordingly, only a weak STAT3 phosphorylation signal was detectable after OSM stimulation, unlike the signal from the majority of healthy control PBMCs (Fig. 4, A and B). Moreover, IL-6-induced STAT3 phosphorylation was consistently slightly reduced in patient PBMCs compared to control, as was IL-31-induced STAT3 phosphorylation, although the response in controls was relatively weak and variable (Fig. 4, C and D). Intriguingly, OSM-stimulated patient PBMCs also expressed significantly lower IL-6 compared to controls, and this effect was rather specific since it was not observed in response to IL-6 nor IL-21 (Fig. 4 E). The signals observed in response to OSM stimulation of PBMCs suggested some degree of OSMR expression in this compartment, although much less than that observed for fibroblasts. Therefore, we next evaluated OSMR expression of various hematopoietic cell types within the PBMC population, including CD4$^+$ and CD8$^+$ T cells (Fig. S4 A) and CD27$^+$ memory B cells (Fig. S4 C), which did not show any OSMR production. This is generally consistent with previous studies (35, 54) and with single-cell gene expression of different leukocyte subsets (55, 56). Although previous reports showed upregulation of OSMR on CD4$^+$ and CD8$^+$ T cells and CD27$^+$ memory B cells by anti-CD3/CD28 activation/stimulation and CpG ODN class B, respectively (35, 54), we did not observe any significant/robust OSMR surface expression on patient nor control T cells after 5 days of anti-CD3/CD28 stimulation (Fig. S4 B) and neither on patient and control B cells stimulated with CpG ODN for up to 9 days (Fig. S4 C). Finally, lipopolysaccharides (LPS) and IFNγ treatment has been reported to induce surface expression of OSMR and IL31RA on monocytes and macrophages (32, 53) giving rise to successful signaling events by OSM and IL-31, respectively. PBMCs were subgated as shown in Fig. 4 F and subsequent flow cytometric analysis revealed OSMR surface expression on monocytes (Fig. 4, G and H) following LPS and IFNγ treatment, whereas OSMR was undetectable on lymphocyte and natural killer (NK) subsets. Surface OSMR expression was significantly higher for monocytes of healthy controls than from the patient (Fig. 4 H). Despite the increased surface expression of monocyte OSMR after LPS+IFNγ pretreatment, which was also reflected in weak STAT3 phosphorylation, this response was only marginally further enhanced in response to OSM treatment (Fig. 4, I and J). Additionally, pretreatment with LPS and IFNγ did not markedly enhance IL-31–induced STAT3 phosphorylation, although this response became detectable in P1 PBMCs (Fig. 4, K and L). Collectively, these data show very modest and selective induction of OSM and IL-31 receptor signaling and capacity to induce STAT3 phosphorylation in the hematopoietic compartment, suggesting that the defective cellular defect in P1 is mainly exerted by the fibroblast/stromal compartment.

B cell–extrinsic elevation of atypical memory B cells, plasma cells and -blasts, and increased IgE class-switch recombination

To evaluate potential defects in the B cell compartment, blood samples were taken from P1 and one healthy control, as well as healthy blood donors, and purified PBMCs were analyzed by FC (Fig. 5, A and B; and Fig. S5 A). P1 displayed a significantly increased frequency of atypical memory B cells (aMBCs), and plasmablasts (PBs) (PBs defined as IgD$^-$CD27$^+$CD20$^-$CD38$^+$) (Fig. 5, A and B). Conversely, significantly fewer conventional MBCs were observed, in agreement with previous observations of a reduction in memory B cells in classical AD-HIES (57). Next, we assayed class-switch recombination (CSR) in the B cell compartment (Fig. 5 C and Fig. S5 B). This revealed an appreciable fraction of IgE-positive cells among the expanded aMBC/PC and PB subsets in the patient, whereas IgE-positive cells could not be detected in the healthy controls, in agreement with the rarity of this subset (58) (Fig. 5 C). To evaluate whether the

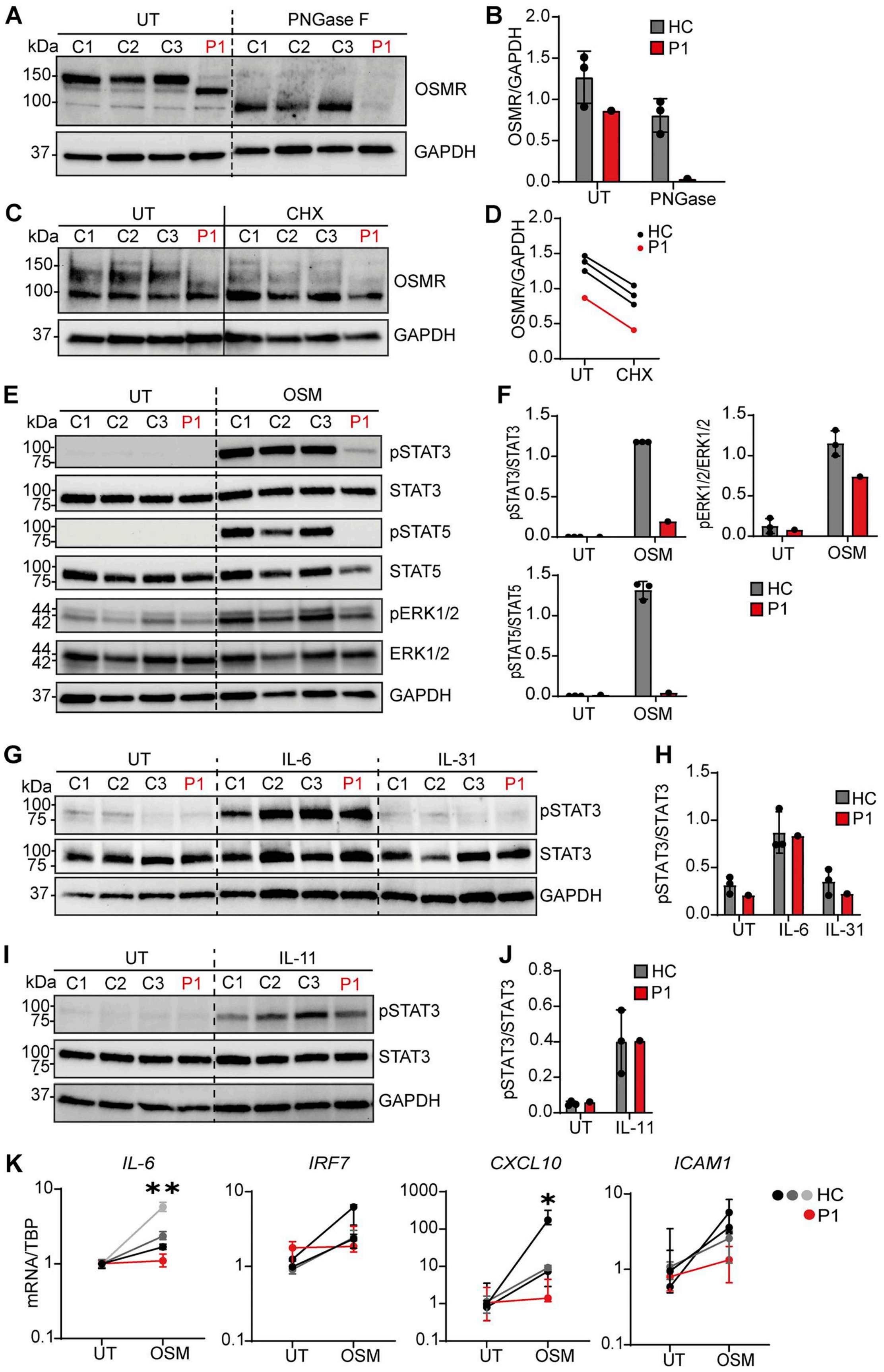

Figure 3. **Patient fibroblasts show different OSMR glycosylation and impaired signaling downstream of OSM. (A)** Endogenous OSMR expression in fibroblast lysates from P1 and three healthy controls (HCs) with or without PNGase treatment. **(B)** Quantification of OSMR band intensities relative to GAPDH

from A. **(C and D)** OSMR production of dermal fibroblasts from P1 and HCs treated with 25 µg/ml protein synthesis inhibitor (cycloheximide, CHX; 1M) for 24 h, and (D) quantification of WT OSMR bands and variant OSMR band intensities relative to GAPDH from C. Experiments shown in A and C were repeated twice with dermal fibroblasts from the patient and three HCs each. **(E and F)** Dermal fibroblasts from P1 and three HCs were stimulated with OSM (5 ng/ml) for 30 min. Whole-cell lysates were harvested for WB for the visualization of pSTAT3, STAT3, pSTAT5, STAT5, pERK1/2, ERK1/2, and GAPDH and quantification of WB band intensities shown in F. **(G–J)** Serum-starved dermal fibroblasts from P1 and three HCs were stimulated with IL-6 (100 ng/ml), IL-31 (100 ng/ml), or IL-11 (100 ng/ml) for 30 min. Whole-cell lysates were harvested for WB (G and I) for the visualization of pSTAT3, STAT3, and GAPDH and band intensities quantitated (H and J). **(K)** Dermal fibroblasts from P1 and HCs were stimulated with OSM (10 ng/ml) for 2 or 6 h. Total RNA was harvested for expression analysis by RT-PCR after 2 h for *IL-6* and after 6 h for *IRF7*, *CXCL10*, and *ICAM1*. Data are representative of three independent experiments performed in quadruplicates. Statistics were calculated using the unpaired *t* test and comparing pooled samples from controls to patient. UT, untreated. * = P < 0.05, ** = P < 0.01. Source data are available for this figure: SourceData F3.

---

observed perturbations in the patient's B cell compartment were B cell intrinsic or extrinsic, we purified untouched naïve B cells by magnet-activated cell sorting and tested their behavior in an induced germinal center B cell (iGB) culture system (Fig. 5 D). This system leverages a normal human dermal fibroblast (NHDF) feeder cell line engineered to express human CD40L in combination with addition of recombinant human IL-21, B cell activating factor (BAFF), and IL-2, and a pulse of IL-4, to drive Th2-like activation, expansion, PB differentiation, and CSR (59). In this system, cells from P1 exhibited slightly lower initial proliferation than the healthy control cells (Fig. 5 E) but differentiated and class-switched to an extent comparable to the control (Fig. 5 F). This demonstrated that naïve B cells from the patient did not harbor any major intrinsic defect. Taken together, our findings suggest a B cell–extrinsic defect in the patient, causing an elevated aMBC/PC and PB frequency with increased IgE class-switching, commensurate with the HIES phenotype.

Complementation with OSMR WT restores OSMR surface expression and OSM-induced STAT3 phosphorylation

To demonstrate conclusively that the aberrant fibroblast phenotype of P1 was attributable to the biallelic OSMR V436D variant, we complemented dermal fibroblasts from P1 with OSMR WT or the OSMR variant by lentiviral transduction (Fig. 6, A–D). Reconstitution of patient fibroblasts with OSMR WT indicated normalization of OSMR glycosylation (upper band in immunoblot Fig. 6 A) as well as STAT3 phosphorylation in response to OSM stimulation (Fig. 6, A and B). Importantly, this effect was not observed when OSMR V436D was overexpressed, neither in the patient nor in healthy control fibroblasts (Fig. 6, A and B). Likewise, reconstitution of patient fibroblasts with OSMR WT also reverted the defect in OSMR surface expression with increasing levels observed exclusively in WT OSMR complemented fibroblasts and not in fibroblasts expressing OSMR V436D variant (Fig. 6, C and D). Collectively, these data demonstrate causality between the OSMR patient variant and impaired OSMR surface expression and abolished STAT3 phosphorylation in patient fibroblasts, suggesting that homozygosity for this novel OSMR variant alters the transcriptomic and phenotypic signature of dermal fibroblasts causing HIES.

Discussion

Here we report a patient with HIES, presenting with atopic dermatitis and eczema, skin and wound infections, and CCPA together with IgE levels up to 34,000 IU/ml, homozygous for a rare variant in *OSMR*. We demonstrate that the patient OSMR V436D variant is deleterious, unlike other homozygous *OSMR* variants with CADD >20 reported in gnomAD, associated with altered N-linked glycosylation, and reduced surface expression of OSMR on patient fibroblasts. Collectively, this result in impaired OSM-induced STAT3 phosphorylation and significantly reduced OSM induction of IL-6 and CXCL10, combined with elevated fractions of IgE-producing PBs and aMBCs in the context of normal Th17 fractions. Reconstitution of patient fibroblasts with OSMR WT restored OSMR expression and functionality, demonstrating that the STAT3 signaling defect observed in fibroblasts is driven by the V436D variant and suggesting disease causality. Utilization of an iGB culture system did not reveal any B cell–intrinsic defect but instead suggested a B cell–extrinsic defect. Based on the clinical history and pathology in the patient, the genetic findings, and the molecular and cellular immunological characterization, we propose that homozygous OSMR deficiency represents a novel genetic etiology of AR-HIES, phenotypically mimicking AD-HIES through an effect upon STAT3 phosphorylation and signaling in fibroblasts.

OSMR deficiency is a novel genetic etiology of HIES, exhibiting a somatic and infectious phenotype reminiscent of AD-HIES caused by DN STAT3 mutations (6, 7), yet with distinctive features and a more narrow phenotype. Despite many similarities, including hyper-IgE, skin infections and poor wound healing, fungal infections, and eczema, together with a somatic phenotype involving abnormalities in bone and teeth, a notable difference between our patient and STAT3 AD-HIES (and AR ZNF341 HIES) is the normal levels of Th17 cells. Any constitutive STAT3 deficiency in hematopoietic cells, being either structural in DN LOF STAT3 variants or due to defective induction of the STAT3 protein in ZNF341 deficiency, compromises Th17 differentiation (22, 60). This discrepancy reveals that OSMR deficiency is similar, but not identical, to AD-STAT3 HIES. A plausible explanation is the more fundamental disturbance of STAT3 signaling downstream of several cytokine receptors, including IL-6, IL-21, TGFβ, OSM, and IL-31 in AD-HIES, caused by DN STAT3 mutations as opposed to select OSMR defect. OSMR belongs to the type I cytokine receptor family, and therefore, it was important to clarify whether other receptor signaling pathways within this family may be affected by the identified deleterious OSMR variant in the patient. For instance, an IL6ST variant was reported to cause cytokine-selective signaling impairment (specifically loss of IL-11 signaling with intact signaling by other IL-6 family cytokines), demonstrating that receptor

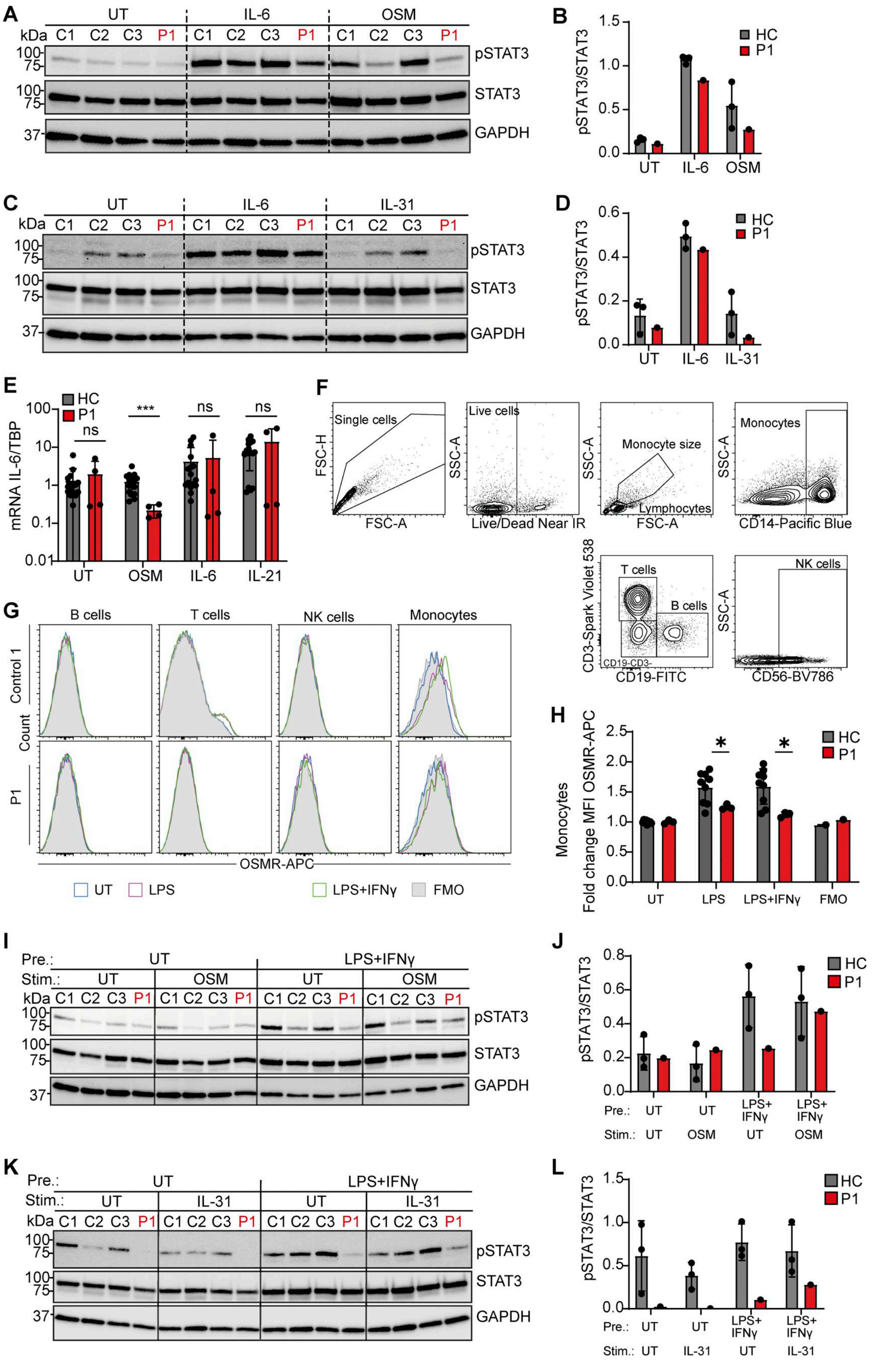

Figure 4. **Constitutive and induced expression and signaling of OSMR in patient and control PBMC populations. (A–D)** Serum-starved PBMCs from P1 and three healthy sex- and age-matched controls were stimulated with IL-6 (100 ng/ml), OSM (100 ng/ml), or IL-31 (100 ng/ml) for 30 min. Whole-cell lysates

were harvested for WB for the visualization of pSTAT3, STAT3, and GAPDH (A and C), and band intensities were quantitated (B and D). **(E)** PBMCs from P1 and three healthy sex- and age-matched controls left untreated (UT) or stimulated with 50 ng/ml OSM, 50 ng/ml IL-6, or 50 ng/ml IL-21 for 6 h. Expression of *IL-6* was measured from mRNA with RT-PCR. Data were analyzed by the double δ Ct method, and statistical differences were determined in GraphPad Prism by unpaired, nonparametric *t* test. **(F)** Gating strategies of control PBMCs stained for T cells (CD3), B cells (CD19), NK cells (CD56), monocytes (CD14), and OSMR and analyzed by FC. **(G)** Representative flow histograms of subpopulations of PBMCs from P1 and three HCs, which were left untreated or treated with LPS (1 µg/ml) alone or LPS (1 µg/ml) + IFNγ (50 ng/ml) for 24 h prior to OSMR surface expression analysis. The grey area (fluorescence minus one, FMO) shows the negative staining control, which represents PBMCs stained with the same staining mixture but without the anti-OSMR Ab as an indicative measure of the background signal. **(H)** Fold change of OSMR surface expression on monocytes (CD14) from LPS- or LPS+IFNγ-treated PBMCs. **(I–L)** PBMCs were pretreated with LPS (1 µg/ml) + 50 ng/ml IFNγ (50 ng/ml) for 24 h prior to stimulation with OSM (100 ng/ml) (I) or IL-31 (100 ng/ml) (K) for 30 min. Whole-cell lysates were harvested for WB for the visualization of pSTAT3, STAT3, and GAPDH, and band intensities were quantitated (J and L). HC, healthy control. Statistics were calculated using the unpaired *t* test. * = P < 0.05; *** = P < 0.001. Source data are available for this figure: SourceData F4.

---

alterations can quantitatively and qualitatively change downstream signaling (61). However, overexpression analysis of patient OSMR V436D in OSMR_LIFR double-defective HEK293 cells did not negatively impact upon STAT3 activation after IL-6 stimulation, indicating that the OSMR V436D variant exclusively disturbs signaling in the receptor complexes OSMR–gp130 and OSMR-IL31RA. This was confirmed by results of IL-6 stimulation of patient fibroblasts and PBMCs, which exhibited similar responses as healthy controls.

Given that the extent of immunological deficiency is also determined by the subsets of cells affected, our finding that OSMR defect almost exclusively affects fibroblast signaling may partially account for the limited degree of cytokine dysregulation, and possibly explain the relatively untouched Th17 cell

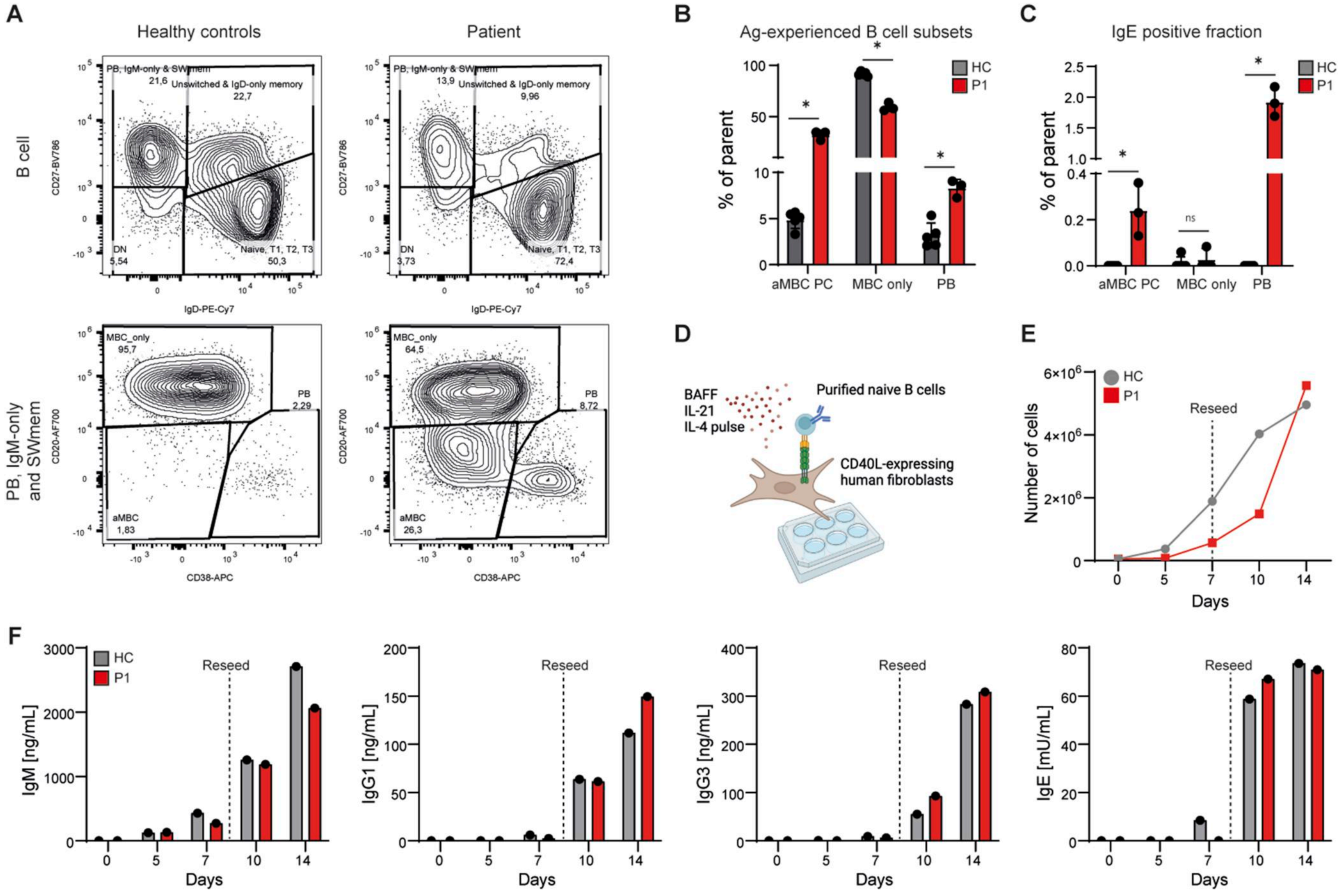

Figure 5. **B cell–extrinsic elevation of circulating plasmablasts and increase in IgE isotype switching in the patient. (A)** Flow plots of main B cell subsets (top row) and antigen-experienced B cell subsets (bottom row) in one healthy control (left panels) and the patient (right panels). Representative of two independent analyses. (Data shown in rows 1 and 2, column 1 are identical to data in Fig. S5 A, row 1, column 4 and 5.) **(B)** Gate frequencies for antigen-experienced B cell subsets of five healthy controls (HCs) and the patient. Representative of two independent analyses. **(C)** Fraction of IgE class-switched cells among antigen-experienced B cell subsets of three healthy controls and the patient. The individual points for healthy control and patient represent one each of three sampling methods (conventional Ficoll prep, separator tubes, and whole-blood RBC lysis) from one experiment. **(D)** Schematic overview of iGB culture setup (created with BioRender). **(E)** Cell counts for one representative of two similar experiments. **(F)** IgM, IgG1, IgG3, and IgE secretion in cultures, normalized to cell count. Full gating strategies are shown in Fig. S5. Statistics were calculated using the unpaired *t* test. * = P < 0.05. aMBC_PC, aMBC/plasma cell; DN, double-negative; MBC_only, conventional memory B cell; SWmem, switched memory; T1, T2, T3, transitional 1, 2, 3 subsets.

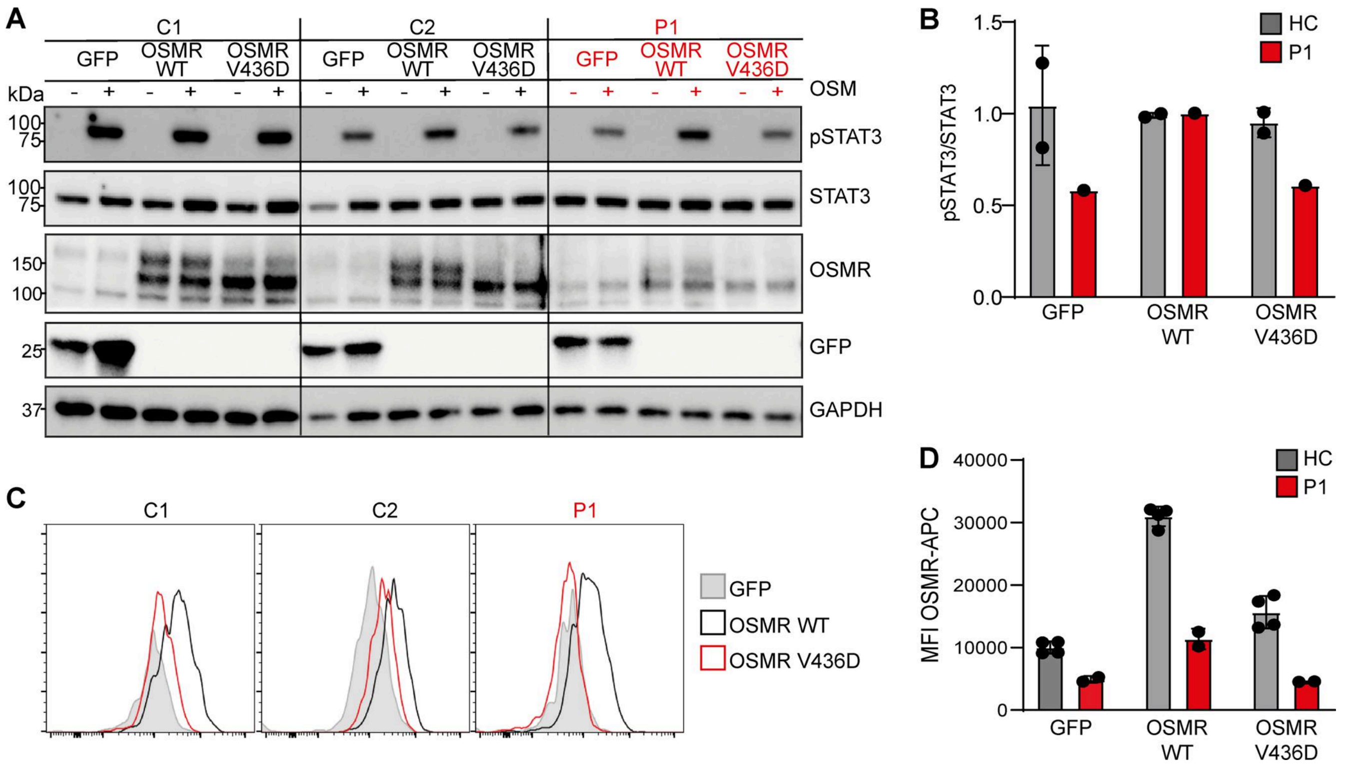

Figure 6. **Reconstitution of patient fibroblasts with WT OSMR restores OSMR surface expression and STAT3 phosphorylation.** Lentiviral transduction of patient dermal fibroblasts with WT and variant OSMR and GFP as transduction control. **(A)** The transduced fibroblasts were stimulated with 5 ng/ml OSM for 30 min, and whole-cell lysates were harvested for immunoblotting for the visualization of pSTAT3, STAT3, OSMR, GFP, and GAPDH, which was used as loading control. **(B)** WB band intensities of pSTAT3/STAT3 from A were determined by ImageJ. **(C and D)** (C) Surface expression of OSMR from the lentiviral transduced fibroblasts was analyzed by FC, and (D) MFI values were plotted. The data shown are representative of three independent experiments performed in duplicates. HC, healthy control; MFI, mean of fluorescence intensities. Source data are available for this figure: SourceData F6.

subsets in the patient. This is because STAT3 signaling in response to other cytokines than OSM and IL-31 is fully preserved in primary patient cells, as also demonstrated by our findings of normal IL-6 and IL-11–induced STAT3 phosphorylation. Indeed, the full HIES phenotype of IL6R defect in AD-HIES suggests that defective IL-6 signaling is one of the key pathogenic features of HIES. Whether the reduction in IL-6 production from OSMR-deficient patient fibroblasts we observed contributes to the observed immunological and clinical phenotype remains unclear. Intriguingly, patients with AR-HIES caused by DN IL6ST deficiency also have preserved Th17 production and seldomly present with skin abscesses and CMC but mostly suffer from abnormalities in bone and teeth (15, 27). Similarly, Th17 production is normal in most patients with AD-HIES caused by STAT6 GOF mutations, whereas T cells show Th2 skewing due to the central role of STAT6 in IL-4 and IL-13 signaling in Th2 cells (17). We did not find Th2 skewing nor increased IL-4 in peripheral blood in the patient, thus leaving the severe atopy and asthma phenotype partly unaccounted for. Altogether, the similarities concerning preserved Th17 fractions may argue for placing AR OSMR deficiency in a functional and immunological category with IL6ST and STAT6 GOF forms of HIES.

Pathological disease manifestations from various tissues, including bone, gingiva/teeth, skin, airways, and blood, collectively support a clinical significance of the identified OSMR deficiency. In relation to bone, the regulation of osteoblast–osteoclast interaction involves OSM, which induces the differentiation of osteoblasts from mesenchymal stem cells via STAT3 (62), while also affecting osteoclast differentiation and subsequent bone resorption (63). It is tempting to attribute the fragility fracture and osteopenia to distorted osteoblast–osteoclast homeostasis, as part of the OSMR deficiency. Fibroblast-expressed OSMR is also involved in tissue repair and remodeling (35, 39), suggesting that the poor wound healing reported by the patient may be directly related to OSMR deficiency. Binding of OSM to fibroblast OSMR induces the production of collagen and other extracellular matrix components as well as proinflammatory cytokines, including IL-6 (39, 64, 65), which may be responsible for some aspects of the immune dysregulation manifested by the patient.

A major finding of significant interest is the observation that OSMR deficiency exhibits a largely fibroblast-confined cellular phenotype, secondarily affecting IgE-producing PBs. It may appear surprising that an immunological phenotype almost exclusively relying on a fibroblast defect can cause such a marked IEI, with not only tissue and bone abnormalities, but also some immune dysregulation and infection. Several points may account for these observations. The fibroblast has gained increasing attention as an important immune modulatory cell (66) not only for innate immunity (67) but also as an immune determinant in B cell–associated germinal center reactivity (68). Especially, fibroblasts serve as essential components of the lymph node microenvironment, supporting lymphocyte migration, localization, and interaction within lymph nodes (69). Fibroblasts can form specialized subsets supporting B and T cell compartmentalization through secretion of various chemokines and cytokines (70). The fact that fibroblasts express OSMR and different leukocyte subsets are important sources of OSM (39), renders it plausible that functional loops between lymph node fibroblasts and lymphocytes exist. This scenario agrees with our data from the iGB culture system, which did not reveal any B cell–intrinsic defect but instead suggested a B cell–extrinsic defect, the latter consisting of abnormal signals from fibroblasts. The elevated levels of circulating, IgE expressing, aMBCs as well as PBs in the patient testified to ongoing germinal center activity, consistent with modestly increased fractions of pTFH. which represent main producers of IL-4 within lymph nodes (71). However, this increased germinal center activity was likely constrained to draining lung lymph nodes, as we, perhaps somewhat surprising, observed no spillover of this activity to the circulation, neither in the form of atopy-biased Th subsets, such as elevated fractions of circulating Th2 or Th9 cells, nor by increased levels of circulating IL-4 or diminished IFNγ levels, respectively. Finally, despite previous reports (55, 56), our data on resting and stimulated patient and control B and T cells (55, 56) did not support the notion that lymphocytes can be induced to express notable levels of OSMR at the cell surface. However, after LPS-IFNγ pretreatment, we did find detectable levels of OSMR surface expression on control monocytes associated with low levels of STAT3 phosphorylation, which was more pronounced in controls than patient PBMCs. It is also notable that the weak OSM-induced STAT3 phosphorylation present in control PBMCs was completely abolished in patient PBMCs. Collectively, we cannot exclude the possibility that OSMR may be expressed at low levels and/or upregulated by blood cells in response to certain stimuli during infection and inflammation, in which context OSMR deficiency may implicate the hematopoietic system.

The present identification of biallelic deleterious *OSMR* variants in a patient with HIES is the first report of homozygous OSMR deficiency. Given that the OSMR V436D variant of the patient is not among the rarest in the general population, and since several other predicted deleterious variants with CADD >20 are found in gnomAD, it was important to establish the true cumulative pLOF of functionally deleterious variants. Indeed, we found that the OSMR V436D variant harbored by the patient is the only functionally defective variant among the 11 identified *OSMR* variants, including variants with higher CADD scores located in the same fibronectin domain as V436D, highlighting the particular relevance of OSMR V436D. Based on our findings of a significantly reduced OSM-induced STAT3 phosphorylation with slight residual signaling in patient fibroblasts as well as in the HEK 293 OSMR_LIFR double KO cell model, the OSMR V436D variant should probably be characterized as hypomorphic rather than complete LOF.

Heterozygosity for OSMR variants affecting the fibronectin domains of the molecule cause AD PLCA, characterized by itchy, thickened, skin with amyloid deposits in the superficial dermis (45, 46, 47). It is hypothesized that distorted IL-31–induced neuronal signaling, mediated through variant OSMR proteins, may elicit the severe pruritus in FPLCA (46). The atopic skin phenotype of our patient, however, did not resemble the one characteristic of FPLCA, defined by grouped hyperkeratotic papules (lichenoid amyloidosis) or macular hyperpigmentation, and notably, a skin biopsy did not reveal amyloid deposits in the dermis in the patient (46). Thus, the disparity in skin manifestations associated with mono- and biallelic OSMR variants, respectively, is intriguing. Recently, a homozygous variant in OSM, reported in a consanguineous family, was associated with inherited severe bone marrow failure syndrome evidenced by profound anemia, thrombocytopenia, and neutropenia, but no increased infection susceptibility (48). This clinical phenotype highlights the importance of OSM for erythro- and myelopoiesis (72), also supported by findings that mice deficient in OSM signaling show mild thrombocytopenia and anemia (45, 73). However, our patient displayed no evidence of bone marrow failure, except for a mild anemia that may also be attributed to long term *Aspergillus* infection. Due to the OSMR defect in our patient, OSM can only signal through variant OSMR–gp130 receptor complexes or the alternative OSM receptor constituted by LIFR and gp130. Since defects in LIFR-gp130 causing Stüve-Wiedemann syndrome is not associated with hematological abnormalities, the absence of affected erythropoiesis and myelopoiesis in our patient is a conundrum, suggesting alternative pathways for OSM to mediate its hematologic effects. The LIFR defect in Stüve-Wiedemann syndrome involves severe skeletal dysplasia, respiratory distress, and dysautonomia, none of which the patient in this paper suffers from. Collectively, based on the phenotype of Stüve-Wiedemann syndrome, defective LIF signaling may be distinguished clinically from defective OSM signaling by the neurological and severe bone-related defects in the former and the cutaneous and hematological defects of the latter (74). Indeed, it has been suggested that craniosynostosis, deciduous teeth, scoliosis, and osteoporosis in HIES are caused mainly by insufficient responses to IL-11 or LIF (75).

Finally, the clinical presentation and cellular phenotype of our patient did share some similarities to patients with dysregulated IL-31RA signaling, such as atopic dermatitis (76) and increased IgE (77, 78), suggesting involvement of defective IL-31–induced OSMR-IL31RA signaling in generation of the clinical phenotype of the patient. Likewise, we would expect IL-31 signaling in patient OSMR V436D cells to be reduced, as was previously documented for another OSMR variant (G618A) located within the second fibronectin domain of OSMR and leading to decreased STAT3 activation in response to both OSM and IL-31 in FPLCA keratinocytes (51). However, we did not have access to any patient cell types in which IL-31R was highly expressed and could therefore not establish the extent of IL-31 signaling defect with certainty. Interestingly, IL-31RA deficiency in mice results in exaggerated Th2-type inflammation in the lungs (77, 78, 79), whereas the patient of the present study did not have elevated peripheral Th2 cell fractions nor increased serum IL-4 levels, perhaps suggesting that any IL31R signaling defect may be modest in the patient given the normal Th2 cell fractions.

Altogether, the specific impact of the OSMR V436D variant downstream of IL31RA/OSMR heterodimer signaling remains to be fully established.

Based on the results of this study, we propose OSMR deficiency as a novel genetic etiology of AR-HIES, closely mimicking the clinical and immunological phenotype of AD-HIES through the influence on STAT3 phosphorylation and activation of downstream effector molecules. The clinical phenotype of OSMR deficiency, however, is distinctive, since the defect is largely restricted to stromal cells/fibroblasts, and IL-6 signaling as well as Th17 subsets are preserved. In particular, this study suggests a selective and almost exclusive role for fibroblasts in mediating the OSMR AR-HIES phenotype. Due to the pleiotropic effects of OSM on mesenchymal cells involved in bone mineralization and immunity, the altered fibroblast gene signature in response to OSM is consistent with the patient's decreased bone mineralization, eczema and skin infection, pulmonary aspergillosis, and an intra-nodal environment conductive to elevated IgE and TFH cell subset formation. Extensive genetic, immunological, and phenotypic variation has been reported in the different forms of AD- and AR-HIES, underscoring the challenge of grouping such heterogeneous disorders by the shared feature of the classic triad of elevated IgE, atopic dermatitis, and recurrent infections. The present study, together with other recent publications, sheds new light on different clinical disease manifestations and immunological phenotypes arising from defective OSMR/gp130/LIFR signaling, manifesting as heterozygous OSMR defect in FPCLA, homozygous OSM defect with congenital hematological bone marrow defect syndrome, or LIFR defect in Stüve-Wiedemann syndrome with neuropathic itching and bone dysplasia.

Despite the data presented here, some issues remain to be reconciled with the existing literature, including the different phenotypes of OSM deficiency and monoallelic OSMR deficiency, which are both distinct from biallelic OSMR deficiency as described here. The identification of additional patients carrying mutations in genes within this pathway, including *OSMR*, *LIFR*, *OSM*, *IL31*, and *IL31R*, as well as careful clinical phenotype description of individuals in large population datasets, will be essential to clarify the underlying molecular mechanisms and phenotypic relationships. As an increasing volume of clinical characteristics and immunological features of HIES are reported, a better understanding of the clinical heterogeneity and complex underlying immunology and pathophysiology emerges. Importantly, this study provides new knowledge with direct medical implications. First, because the diverse organ manifestations deriving from bone, skin, and lungs present diagnostic challenges and point to more complex ways, in which OSM and IL-31 mediate their physiologic effects. Second, as we suggest that *OSMR* should be part of the panel of genes investigated in patients with a clinical phenotype involving features of atopy and HIES. Undoubtedly, additional genetic etiologies remain to be identified and characterized to provide a more comprehensive picture of this intriguing condition and the associated immune dysregulation predisposing to elevated IgE and atopy with staphylococcal and fungal infections in skin and lungs in humans.

Materials and methods

Full clinical history of a 57-year-old male patient with eczema, asthma, skin infections, and CCPA

We investigated a 57-year-old man of Caucasian (Danish) descent with a clinical history of severe atopic dermatitis, eczema, and asthma throughout life. He experienced slow wound healing and frequent secondary staphylococcal skin infections and pustules, but only seldomly skin abscesses. Dental status was poor with tooth retraction at a young age and a previous history of a tooth abscess (Fig. 1 A). From the age of 20 years, he experienced one or more bacterial pneumonias per year, as well as episodes of oral candidiasis but not CMC or invasive candida infection. At the age of 45 years, he had a distal radial fracture in response to a low energy trauma, a subsequent bone density scan showing osteopenia, originally presumed to be related to prolonged steroid therapy for his asthma. Due to prolonged coughing, dyspnea and chest pain he was referred to the Department of Pulmonology on suspicion of lung cancer. However, computed tomography of the chest showed signs of chronic pulmonary aspergillosis with a thick-walled cavity in the left upper lobe characteristic of an aspergilloma (Fig 1 B). Bronchoscopy revealed *A. fumigatus* DNA and a positive AGA (AGA: 1.9). Blood tests at that time showed increased *Aspergillus* IgG (IgG;157 mg/L, normal range <26.9 mg/L) and IgE (37,900 IU/L, normal range <350 IU/L), slightly increased eosinophil count (0.66 × 109/L, normal range <0.5 × 109/L), and a very high IgE (IgE: 34,000 × 103 IU/L, normal range <100 IU/L) (Table S1). A diagnosis of chronic cavitary pulmonary aspergillosis (CCPA) was established and the patient was treated with itraconazole for 8 mo. Due to disease progression, he was changed to voriconazole for 3 mo, but due to side effects changed again to posaconazole and after 1.5 years of therapy symptoms became stable and stopped therapy. Due to recurrent pneumonia during follow-up, he was started on prophylactic sulfamethoxazole and trimethoprim (Bactrim) prophylaxis. Clinical immunological evaluation and immune phenotyping. A skin biopsy showed perivascular inflammation consisting of lymphocytes and eosinophils but no amyloid deposits.

Results of clinical immunological evaluation

Standard immunological screening revealed normal serum concentrations of IgA, IgM, and IgG (including IgG subclasses) (Table S1). Serum IgE was markedly elevated to levels ranging from 18,200 to 34,000 IU/ml. (Fig. S1 and Table S1). Recurrent monocytosis and mild eosinophilia, interpreted as secondary to CCPA, was also noted (Table S1). Representative hematology values showed mild normocytic anemia in the range of between 6.8 and 7.8 mmol/L (normal range 8.3–10.5 mmol/L, but normal platelet and leukocyte concentrations) (Table S1). Peripheral $CD19^+$, $CD4^+$, and $CD8^+$ lymphocyte concentrations were normal; however, patient $CD4^+$ T cells displayed an activated ($HLA\text{-}DR^+$: 30%) phenotype (Table S1). Lymphocyte subset analysis showed normal distributions of naïve and memory $CD19^+$, $CD4^+$, and $CD8^+$ lymphocytes, respectively, as well as normal Th2 ($CD4^+$ $IL\text{-}4R\alpha^+$), Th9 ($CD4^+$ $CXCR3^+$ $CCR4^-$ $CCR6^+$), and Th17 ($CD4^+$ $CD161^+$ $CCR4^+$ $CCR6^+$) subsets, except for slightly elevated pTFH cell ($CD4^+$ $CXCR5^+$ $PD1^+$ $ICOS^+$) frequencies in the patient (Table S1 and Fig. S2), the latter consistent with the patient's marked ongoing IgE response. Serum levels of IL-4 and IFNγ were likewise within normal ranges. In response to anti-CD3/CD28 stimulation, patient CD4$^+$ T cells displayed similar proliferation characteristics as those of controls (Fig. S3 B). Patient CD8$^+$ T cells responded more indolent to CD3/CD28 stimulation than control CD8$^+$ T cells, as evidenced by a reduced proliferation index and a diminished responding fraction (Table S1). Stimulated patient CD4$^+$ T cells displayed no relative expansion of Th2 cells (CD4$^+$ IL-4Rα$^+$ T cells) compared to those of controls (Fig. S3 B). The patient's vaccination titers to diphtheria, tetanus, and pneumococcal (23-valent polysaccharide) vaccines were normal.

Patient inclusion and patient material

The patient was included in the study by written consent. Whole blood samples were obtained in lithium heparin tubes for WGS and PBMC isolation by Ficoll density gradient centrifugation using SepMate PBMC isolation tubes (#86460; STEMCELL Technologies) and frozen in liquid nitrogen at the Department of Clinical Immunology, Odense University Hospital (Odense, Denmark). Control PBMCs were purified from healthy donors after obtaining written consent at Department of Biomedicine, Aarhus University (Aarhus, Denmark). A skin biopsy from the patient was taken under local anesthesia, and dermal fibroblasts were subcultured at the Department of Clinical Immunology, Odense University Hospital (Odense, Denmark). NHDFs were obtained from PromoCell.

Ethics

The patient and healthy controls were included following oral and written consent in accordance with The Helsinki Declaration and national ethics guidelines and after approval from the Danish National Committee on Health Ethics (1-16-02-621-16), the Data Protection Agency, and Institutional Review Board.

WGS and genetic data analysis

DNA was extracted from 400 µl blood using the QIAsymphony DSP DNA Midi Kit with an elution volume of 100 µl. The DNA concentration was measured with Qubit dsDNA BR. An input of 300 ng DNA was used for library preparation using the Illumina DNA PCR-Free Prep. The library was sequenced on an Illumina NovaSeq 6000 with a S4 flow cell using 2 × 150 bp paired ends sequencing. The paired end reads were mapped to the hg38 reference genome with bwa mem v0.7.15 (80, *Preprint*), duplicate reads were flagged with Picard v2.21.9 MarkDuplicates (https://github.com/broadinstitute/picard), and variants were called using GATK v4.1.9.0 HaplotypeCaller (https://github.com/broadinstitute/gatk). The mapped reads resulted in a median coverage of 40×.

Variant filtration and classification strategy

VarSeq software (version 2.3.0, Golden Helix, Inc.) was used for annotation and filtering of variants. Population frequency (gnomAD Exomes Variant frequencies version 2.0.1, Broad Institute) threshold was set to 1% to exclude common polymorphisms. In addition, sequence ontology was applied so only non-synonymous variants in coding regions of genes or variants, including structural variants predicted to affect translation, were considered. Variants were classified using American College of Medical Genetics and Genomics criteria (81) in part based on annotations, including CADD version 1.5 score (82), gnomAD frequency, ClinVar submission interpretations, and HGMD Pro version 2022.4 variant classification. The MSC of CADD value with 95% confidence interval was determined by Zhang et al. (83). The cumulative pLOF was calculated by summarizing all allele frequencies (from gnomAD version 4.1.0) from the respective gene. The gene damaging index (GDI-Phred) was determined by Itan et al. (84).

We have investigated the presence of genetic variants in introns and exons, including 5′ and 3′ UTR and promoter sequences, of the following genes*: AIRE*, *CARD9*, *CARD11*, *CARMIL2/RLTPR*, *DOCK8*, *ERBIN*, *FOXP3*, *IL6R*, *IL6ST*, *IL12RB1*, *IL17RA*, *IL33*, *LRBA*, *PEPD*, *PGM3*, *SMAD3*, *SPINK5*, *STAT1*, *STAT3*, *STAT6*, *TGFBR1*, *TGFBR2*, *WAS*, and *ZNF341.* This list comprises genes associated with HIES based on The International Union of Immunological Societies Expert Committee (85) and genes associated with the phenotype HIES in the Human Gene Mutation Database variant database. Genetic analysis of these genes revealed a monoallelic deletion in intron 1 of the *SMAD3* gene with a frequency of 0.4477 in the gnomAD and DECIPHER databases. This variant was assessed not to be causal of the patient phenotype due to the high frequency in the healthy population. No other copy number variations were identified in the aforementioned genes.

We further identified 68 variants with allele frequency <0.01. Filtration for CADD >15 reduced the list to four monoallelic variants: a missense variant NM_203447.4:c.380G>A, NP_982272.2:p.Arg127His in *DOCK8*, a missense variant NM_001282933.2:c.2309C>T, NP_001269862.1:p.Pro770Leu in *ZNF341,* an in-frame deletion c. NM_014339.7:c.2446_2454delGAAGAGGAG, NP_055154.3:p.Glu816_Glu818del in *IL17RA*, and the missense variant in *OSMR* described in the manuscript. We ruled the *DOCK8* variant as not causal, since HIES is primarily described in patients with homozygous DOCK8 deficiency, and this specific variant has been found in >700 healthy heterozygous individuals in the gnomAD database. In addition, the patient did not have an increased number of CD45RA$^+$CD8$^+$ T cells, which is inconsistent with DOCK8 deficiency. Variants in *ZNF341* are, like *DOCK8* variants, known to cause HIES with AR inheritance. HIES due to *ZNF341* variants is characterized by increased IgG, increased number of naïve B cells, alopecia, aphthous stomatitis, food allergy, and syndromal features, neither of which is present in the patient (21, 22). Finally, the patient has normal STAT3 phosphorylation in response to IL-6 stimulation (Fig. 3, G and H; and Fig. 4, A–D), which is not consistent with either DOCK8 or ZNF341 deficiency (21, 86). The variant in *IL17RA* is located close to the 3′end of the gene, has been identified in over 600 healthy heterozygous individuals in the GnomAD database, and the patient phenotype has limited overlap with IL17RA deficiency (87). Therefore, we also ruled out that this variant as causal of the patient phenotype. The 64 variants filtered out by CADD >15 are intronic variants. These variants were assessed using the splicing prediction tools GeneSplicer, MaxEntScan, NNSplice, and

NCBI's Position Weight Matrix. Only one of these variants, present in the *LRBA* gene, was predicted by three out of four tools to introduce a cryptic splice site. However, as LRBA-associated HIES follows recessive inheritance, this intron variant was considered not to be the causal variant.

Overexpressing GFP, OSMR WT, and predicted deleterious *OSMR* variants in HEK293 cells by plasmid transfection

Plasmids with *OSMR* WT and *OSMR* variants were purchased and cloned in the vector pGenLenti by GenScript. The plasmids containing the different *OSMR* variants were validated by sequencing. GFP was used for transfection control and was overexpressed on pCCL/PGK-eGFP plasmid. For transfection, 20,000 HEK cells were seeded in a 48-well plate one day prior to transfection. On the transfection day, 100 ng plasmid DNA (122 ng plasmid for the plasmid containing WT *OSMR*) were mixed with up to 10 µl OPTI-MEM, and in another tube, 0.4 µl of the transfection reagent PEI (24765; PEI MAX - Transfection Grade Linear Polyethylenimine Hydrochloride [MW 40,000]) was mixed with 9.6 µl OPTI-MEM. These two tubes were separately incubated at room temperature (RT) for 5 min before they were pooled and followed by another incubation of 20 min at RT. Hereafter, the transfection mix was ready to be gently added to the respective cells. The best OSMR production in HEK cells was achieved after 48 h, which was shown by WB.

Flow cytometric lymphocyte characterization

The following primary conjugated (anti-human) antibody specificities were used (BD): CD3 (FITC; PerCP-Cy5-5), CD4 (APC; PE-Cy7), CD8 (APC; APC-Cy7), $CD16^+$CD56 (PE), CD19 (APC; PerCP-Cy5.5), CD27 (PE), IgD (FITC), κ-light chain (FITC), λ-light chain (PE), IgG1 κ-light chain isotype (mouse) (FITC), CD45 (PerCP-Cy5. 5), CD45RA (FITC), CD45RO (PE), HLA-DR (APC), TCRαβ (FITC), TCRγδ (PE), CD161 (FITC), CD183 (CXCR3, BV510), CD185 (CXCR5, PerCP-Cy5.5), CD194 (CCR4, PE), CD196 (CCR6, APC), CD278 (ICOS, BV421), and CD279 (PD1, PE). For analysis of intracellular IL-17A and OSMR surface expression, the anti-human FITC IL-17A and the APC-conjugated OSMR antibodies, both from (Thermo Fisher Scientific), were used. All samples were analyzed on a FACS Canto II (BD).

T cell stimulation

Cryopreserved PBMC were thawed and rested (in a 37°C incubator with 5% CO_2) in culture medium (RPMI 1640 + 10% AB serum) overnight. Next day, CFSE-stained PBMC were left unstimulated or stimulated with anti-CD3/CD28 Dynabeads (Thermo Fisher Scientific) in 96-well plates for 5 days according to the manufacturer's instructions. The supernatants were harvested and proliferation of $CD4^+$ and $CD8^+$ T cells (2–4 wells containing 100,000 cells/well were pooled) as well as OSMR and IL-4Rα surface expression was ascertained. T cell proliferation was evaluated by two parameters: Proliferation index: mean number of cell divisions among the responding fraction (responding fraction: fraction of T cells undergoing at least one cell division [%]).

Intracellular IL-17A staining

Cryopreserved PBMC were thawed and left overnight in culture medium. Monensin solution (Thermo Fisher Scientific) (dilution 1:1,000) was added to PBMC cultures (1 × 10^6 cells/ml), which were then left unstimulated or stimulated with PMA (15.4 ng/ml, Merck, KGaA) and ionomycin (300 ng/ml, Thermo Fisher Scientific) for 4 h. Anti-CD4 surface-stained PMBC were fixed and permeabilized (FoxP3/Transcription kit, Thermo Fisher Scientific) and stained for intracellular IL-17A followed by flow cytometric analysis.

In vitro stimulation of primary dermal fibroblasts for western blotting

NHDFs were seeded 1 day prior to stimuli/transfection in DMEM supplemented with 10% FCS and 1% Pen/strep (P/S). For WB, NHDFs were stimulated with 5 ng/ml OSM or 100 ng/ml IL-6 for 30 min and immediately put on ice. Cells were lysed and prepared for WB as detailed in supplementary methods. For RT-PCR, NHDFs were stimulated with 10 ng/ml OSM for 2 or 6 h mRNA was extracted according to manufacturer (#740466.4; MACHEREY-NAGEL).

In vitro stimulation of primary dermal fibroblasts and PBMCs for western blotting

Primary dermal fibroblasts were seeded in a 24-well plate with 25,000 cells per well. If the duration of the experiment would be <2 days, the DMEM was supplemented with 10% FCS and 1% P/S, and if the duration was >2 days, the DMEM was supplemented with 2% FCS and 1% P/S. Cells were always seeded 1 day prior to stimuli/transfection. PBMCs were seeded in RPMI supplemented with 1% FCS and 1% P/S with 500,000 cells per well. Fibroblasts were stimulated for 30 min with 5 ng/ml OSM (Human Oncostatin M [209 aa] Recombinant Protein, #300-10T-10UG; PeproTech) and immediately put on ice. For IL-6 and IL-31 stimulation of fibroblasts, cells were seeded in medium containing 1% FCS one day prior to stimulation. Cells were stimulated for 30 min with 100 ng/ml IL-6 (#200-06-5UG; PeproTech) IL-31 (#200-31-2UG; PeproTech) or 10 ng/ml IL-11 (#200-11-2UG; PeproTech) and immediately put on ice. PBMCs were stimulated with 100 ng/ml OSM, IL-6, or IL-31 for 30 min and immediately put on ice. PBMCs were pretreated with either 1 µg/ml LPS (from *Escherichia coli* O26:B6, L2654-1MG; Millipore Sigma) or 50 ng/ml IFNγ (Recombinant Human IFN-γ, #300-02; PeproTech) for 24 h prior to stimulation.

Western blotting

Whole-cell lysates were generated by washing the cells with ice-cold PBS and lysed in Ripa buffer (Thermo Fisher Scientific) supplemented with PhosSTOP (Merck) and Complete Ultra protease inhibitor (Roche), Sodium fluoride (Avantar), and Benzonase Nuclease (Sigma-Aldrich) for 5 min on ice and stored at −20°C. Protein concentrations were measured using Pierce BCA protein Assay Kit (#23223; Thermo Fisher Scientific). Cell lysates were denatured at 95°C for 5 min with 50 mM DTT (#43816-10ML; Sigma-Aldrich) and 4×Laemmli buffer (#1610747; Bio-Rad). Samples were loaded together with Precision Plus Protein Dual Color Standard protein marker (Bio-Rad) onto a Criterion TGX Precast Midi Protein Gel in Nu PAGE MOPS SDS running buffer (NP0001; Thermo Fisher Scientific). Proteins were transferred onto a Trans-Blot Turbo

Midi Polyvinylidene Fluoride (PVDF) Transfer membrane (Bio-Rad) using the Trans-Blot Turbo Transfer System (Bio-Rad). Membranes were washed using Tris-buffered saline (Thermo Fisher Scientific) supplemented with 0.05% (vol/vol) Tween 20 (Sigma-Aldrich) (TBS-T), blocked for 1 h at RT in 5% Bovine Serum Albumin (BSA, Sigma-Aldrich) in TBS-T, washed with TBS-T three times for 5 min each, and incubated overnight (o/n) at 4°C with primary antibody diluted 1:1,000 in 5% BSA in TBS-T with 0.05% Sodium Azide. The following morning, membranes were washed with TBS-T three times for 5 min each, incubated for 1 h with secondary antibody diluted 1:10,000 in 5% Skim Milk Powder (Sigma-Aldrich), washed five times for 5 min each, and proteins were visualized using Clarity Western ECL Substrate (Bio-Rad) or Clarity Max Western ECL substrate (Bio-Rad) on a ChemiDoc Imaging system (Bio-Rad). To visualize other proteins (for instance non-phosphorylated proteins) at or close to the initial visualized protein (for instance phosphorylated proteins), the membrane was stripped in Restore Western Blot Stripping Buffer (21059; Thermo Fisher Scientific) according to the manufacturer's protocol prior to blocking, washing, and finally o/n incubation at 4°C in primary antibody solution.

The following primary antibodies were used: anti-pSTAT3 (pTyr705, cat. no. 612356; BD Biosciences), anti-STAT3 (cat. no. 610189; BD Biosciences), anti-pSTAT5 (pTyr694, cat. no. 611964; BD Biosciences), anti-STAT5 (cat. no. 610191; BD Biosciences), pERK1/2 (pThr202/pTyr204, phospho-p44/42 MAPK, cat. no. CST-9101S; BioNordika), ERK1/2 (p44/42 MAPK, cat. no. CST-9102S; BioNordika), anti-OSMR (cat. no. CST-95443; BioNordika), anti-GFP (cat. no. NB600-308SS; Novus Biologicals), anti-GAPDH (cat. no. ab9485; Abcam), and anti-Vinculin (rabbit, cat. no. CST-13901; Cell Signaling Technology). As secondary antibodies, peroxidase-conjugated donkey-anti-rabbit and donkey-anti-mouse were used (711-036-152 and 715-036-150; Jackson ImmunoResearch). Specific bands were quantified by densitometry using the Image J software.

RT-PCR

RNA was extracted from lysed cells using NucleoSpin 96 RNA Core Kit (#740466.4; MACHEREY-NAGEL), according to the manufacturer's instructions and eluted in 75 µl RNase-free H2O. Quantitative RT-PCR was performed with TaqMan RNA-to-CT 1-Step Kit (#4392938; Thermo Fisher Scientific) using probes targeting TATA-box binding protein (TBP, #Hs00427620_m1; Thermo Fisher Scientific), CXCL10 (#Hs01124251_g1; Thermo Fisher Scientific), IL-6 (#Hs00985639_m1; Thermo Fisher Scientific), ICAM1 (#Hs00164932_m1; Thermo Fisher Scientific), and IRF7 (#Hs01014809_g1; Thermo Fisher Scientific), according to the manufacturer's instructions. A QuantStudio 3 Real-Time PCR System (Applied Biosystems) was used for quantification of RNA levels relative to the expression of TBP using the $2^{-\Delta\Delta Ct}$ method (88), and the expression levels were normalized to the controls.

B cell phenotyping

Processing of blood and buffy coats

Patient and control (matched for sex and age) PBMCs were isolated from lithium-heparin-stabilized blood obtained following informed consent. Additional blood donor control PBMCs were purified from buffy coats obtained from anonymized healthy blood donors at the blood bank of Aarhus University Hospital, Denmark. Whole blood or buffy coat was diluted 1:1 with PBS, and PBMCs were isolated by a Ficoll-Paque PLUS (GE Healthcare) density gradient centrifugation using SepMate tubes (STEMCELL Technologies) with centrifugation at 1,200 *g* for 10 min at 20°C. The PBMCs were subsequently washed in PBS, centrifuged at 500 *g* for 10 min at 20°C, then incubated in PBS with 27 mM EDTA for 5 min at RT before centrifugation at 300 *g* for 8 min at 20°C, followed by another wash in PBS. For CSR analyses of PB, plasma cell and memory subsets, alternative sample preparation methods were assayed, including conventional Ficoll-Paque separation without SepMate tubes, as well as direct whole-blood erythrocyte lysis using RBC lysis buffer (155 mM NH_4Cl, 12 mM $NaHCO_3$, and 0.1 mM EDTA).

Purification of untouched naïve B cells

For the magnetic isolation of human naïve B cells, purified PBMCs were resuspended in 5 ml magnetic-activated cell sorting (MACS) buffer (PBS, 2% heat-inactivated fetal bovine serum [FBS], and 2 mM EDTA) at RT, before being counted, and then incubated 5 min on ice with Human BD Fc block (Clone Fc1, 564220; BD). Miltenyi Biotec Human Naïve B Cell Isolation biotin-antibody cocktail (130-091-150) was then added for another 30-min incubation. The samples were then diluted with MACS buffer and centrifuged at 200 *g* 10 min at 4°C. The pellet was resuspended in 1 ml MACS and incubated 20 min with Miltenyi Biotec anti-biotin magnetic beads, pre-diluted in 2 ml MACS buffer. The cell suspension was loaded onto pre-wetted Miltenyi Biotec LS columns through 70-µm cell strainers and washed two times with 3 ml MACS buffer. Collected flow-through of untouched human naïve B cells ($CD19^+$, $CD20^+$, $CD22^+$, $CD27^-$, and IgD^+) was validated using FC. Cell aliquots of human B cells were frozen in freeze medium (90% FBS and 10% DMSO) using Corning CoolCell containers as recommended by the manufacturer.

iGB co-culture system

CD40L-expressing NHDF feeder cells (kindly provided by Anne Rovsing and Jakob Giehm Mikkelsen, both Department of Biomedicine, Aarhus University, Aarhus, Denmark [59]) were passaged at least 8 days before being seeded and incubated in B cell medium (BCM; RPMI-1640 [+] L-Glutamine supplemented with 55 µM 2-Mercaptoethanol, 1% P/S, 10 mM HEPES, and 1 mM Sodium Pyruvate [all Invitrogen]) and 10% FBS. The following day (day 0), purified naïve B cells were seeded onto the feeder cells in BCM supplemented with recombinant human IL-4 (10 ng/ml), IL-21 (10 ng/ml), BAFF (10 ng/ml), and IL-2 (50 ng/ml) (#200-04, 200-21, 310-13, and 200-02, respectively; all from Peprotech). On day 3 and 5, half the culture volume of medium was exchanged with fresh BCM similarly supplemented with IL-21, BAFF and IL-2, but no IL-4. On day 7, B cells were harvested then subjected to the analysis of interest or reseeded on fresh feeder cells. Culture supernatants were stored with 0.1% NaN_3 for later time-resolved immunofluorometric assay (TRIFMA) analysis of secreted antibody isotypes as described below, and cell pellets were frozen in freeze medium for analysis by FC.

Flow cytometry analysis

Cell suspensions of interest were prepared in FC buffer (PBS with 2% FBS and 1 mM EDTA), and 100 μL of sample was added 20 μl Human BD Fc Block (Clone Fc1, 564220; BD, pre-diluted 1/50), then preincubated for 5–10 min. Then 100 μl fluorophore-conjugated antibody panel of choice (see below) diluted in a 1:1 mix of FC buffer with Brilliant Stain buffer (563794; DB) was added. After 30 min of staining on ice, the cells were washed and subsequently resuspended in FC buffer.

Panel for B cell phenotyping included: Mouse α-human CD11c-BV421 (Clone BU15, 566877; BD), Mouse α-human CD3-BV510 (Clone OKT3, 566780; BD), Mouse α-human IgM-BV605 (Clone G20-127, 562977; BD), Mouse α-human CD21-BV711 (B-ly4, 563163; BD), Mouse α-human CD27-BV786 (Clone L128, 563327; BD), Mouse α-human CD16-FITC (Clone 3G8, 555406; BD), Mouse α-human CD8-PerCP/Cy5.5 (Clone SK1, 565310; BD), Mouse α-human CD19-PE (Clone HIB19, 555413; BD), Mouse α-human CD24-PE-CF594 (Clone ML5, 562405; BD), Mouse α-human TCRβ-PE-Cy5 (Clone IP26, 306710; BioLegend), Mouse α-human IgD-PE-Cy7 (Clone IA6-2, 561314; BD), Mouse α-human CD38-APC (Clone HIT2, 555462; BD), (Clone DX2, 561976; BD), Mouse α-human CD20-AF700 (Clone 2H7, 560631; BD), and Viability Dye eFluor 780 (65-0865-14; eBioscience). All antibodies were diluted 1/250, except for anti-IgM, which was diluted 1/125, and viability dye, which was diluted 1/2,000.

Panel for CSR analysis was: Mouse α-human CD11c-BV421 (Clone BU15, 566877; BD), Mouse α-human IgE-BV510 (Clone G7-26, 744316; BD), Mouse α-human IgM-BV605 (Clone G20-127, 562977; BD), Mouse α-human CD21-BV711 (B-ly4, 563163; BD), Mouse α-human CD27-BV786 (Clone L128, 563327; BD), F(ab')$_2$-Goat α-human IgA-FITC (polyclonal, H14101; Invitrogen), Mouse α-human CD138-PerCP/Cy5.5 (Clone MI15, 564605; BD), Mouse α-human CD19-PE (Clone HIB19, 555413; BD), Mouse α-human CD24-PE-CF594 (Clone ML5, 562405; BD), Mouse α-human IgG-PE-Cy5 (Clone G18-145, 551497; BD), Mouse α-human IgD-PE-Cy7 (Clone IA6-2, 561314; BD), Mouse α-human CD38-APC (Clone HIT2, 555462; BD), (Clone DX2, 561976; BD), Mouse α-human CD20-AF700 (Clone 2H7, 560631; BD), and Viability Dye eFluor 780 (65-0865-14; eBioscience). All antibodies were diluted 1/250, except for anti-IgM, which was diluted 1/125, and viability dye, which was diluted 1/2,000. All antibodies were included in initial stain with viability dye. Following incubation and wash, the cells were fixed and permeabilized using eBioscience Foxp3/Transcription Factor Staining Buffer Set (00-5523-00; Thermo Fisher Scientific) according to the manufacturer's instructions and restained for intracellular immunoglobulins (IgM, IgD, IgG, IgA, and IgE) before analysis. The stained cell solutions were analyzed on a NovoCyte Quanteon 4025 (Agilent) cytometer equipped with four lasers (405, 488, 561, and 640 nm) and 25 detectors. The acquired data were analyzed using FlowJo v. 10.10.0 (BD).

TRIFMAs of cell culture supernatants

To quantify secretion of antibody isotypes, TRIFMAs were performed on culture supernatants. Wells of FluoroNunc MaxiSorp 96-well plates were coated with 100 μl capture antibody diluted in PBS, either 0.5 μg/ml goat α-human IgM-Hc (2023-01; Southern Biotech), 5 μg/ml mouse α-human IgG1-Fc (9054-01; Southern Biotech), 1 μg/ml mouse α-human IgG3-hinge (9210-01; Southern Biotech), or 2.5 μg/ml mouse α-human IgE-Fc (9240-01; Southern Biotech). Plates were incubated o/n at 4°C, then emptied and blocked with 200 μl TBS (137 mM NaCl, 2.7 mM KCl, and 25 mM Tris/Tris-HCl containing 0.09% [wol/vol] sodium azide [BP2471-500; Thermo Fisher Scientific]) with 1% BSA (A4503; Sigma-Aldrich) for 1 h at RT and washed three times with TBS containing 0.05% (vol/vol) Tween-20 (TBS/Tw). Supernatants were diluted 1/5 in TBS/Tw/0.1% BSA and added in duplicates to wells, then incubated 2 h at RT. Standard curves were prepared in TBS/Tw/0.1% BSA as serial dilutions of either human IgM (0158L-01; Southern Biotech) starting at 300 ng/ml and further eight times threefold dilution; human IgG1 (0151-K; Southern Biotech) starting at 450 ng/ml and further eight times threefold dilutions; human IgG3 (0153-L; Southern Biotech) starting at 50 ng/ml and further eight times threefold dilutions; or for human IgE, human donor plasma starting at threefold dilution and further eight times 2.5-fold dilutions. Following incubation, wells were washed three times with TBS/Tw before addition of detection antibody diluted in TBS/Tw, biotinylated goat anti-human IgG(H+L) (2016-08; Southern Biotech) 0.5 μg/ml for IgM detection, biotinylated goat anti-human IgG(H+L) (2016-08; Southern Biotech) 0.1 μg/ml for IgG1-and IgG3-detection, and biotinylated mouse anti-human IgE-Fc (9250-08; Southern Biotech) 0.2 μg/ml for IgE detection. After 2-h incubation, wells were emptied and washed three times in TBS/Tw, then incubated 30 min at RT with 100 μl/well Eu^{3+}-labeled streptavidin (1244-360; PerkinElmer) diluted to 1 μg/ml in TBS/Tw containing 25 μM EDTA. Lastly, wells were washed three times with TBS/Tw and added 200 μl Enhancement solution (Ampliqon). Plates were shaken 5 min and measured on a time-resolved fluorometry plate reader (Victor X5 Perkin Elmer). Concentrations were derived by interpolation on standard curves fitted using 5-parameter fit in WorkOut 2.5, then normalized to cell counts and expressed as ng/ml (IgM, IgG1, IgG3) or milli-units (mU)/ml (IgE) per 100,000 cells.

Generation of *OSMR* expression constructs

Coding sequences of OSMR and OSMR c.1307T > A were PCR-amplified from an OSMR-encoding plasmid (RC216943; OriGene) using the primers 5′-CGGGCCTTTCGACCTCTAGCGGGATCCGCCGCGCCGCCACCCGCGATCGC-3′ and 5′-CCAGAGGTTGATTATCGGAATTCCCTCGAGGGCGGCCGCGTACGCGTCGGTCCGCTGC-3′ or 5′-CGGGCCTTTCGACCTCTAGCGGGATCCGCCGCGCCGCCACCCGCGATCGC-3′, 5′-CCAGAGGTTGATTATCGGAATTCCCTCGAGGGCGGCCGCGTACGCGTCGGTCCGCTGC-3′, 5′-CTCACAATTCTCCAGTCATCAGGGGCCTCTG-3′ and 5′-CAGAGGCCCCTGATGACTGGAGAATTGTGAG-3′. The PCR-fragments were inserted into BamHI/XhoI-digested pCCL/PGK-eGFP using NEBuilder HiFi DNA Assembly Cloning Kit (New England Biolabs) according to the manufacturer's protocol. The resulting plasmids were designated pCCL/PGK-OSMR and pCCL/PGK-OSMR c.1307T > A. Both inserts were verified by Sanger sequencing.

Lentiviral production and transduction

Third-generation lentiviral vectors were produced as previously described (89). Briefly, HEK293T cells were transfected with 11.25 µg pMD.2G, 9 µg pRSV-Rev, 39 µg pMDLg/pRRE, and 39 µg lentiviral transfer vector for T175 flasks with a surface area of 175 cm^2 using a standard polyethyleneimine transfection protocol. 6 h after transfection, the medium was changed. 2 days after transfection, viral supernatants were poured into tubes and kept in fridge, and cells received fresh medium to produce more virus. Three days after transfection viral supernatants from day 2 and 3 were pooled, filtrated and titrated by quantification of the number of lentiviral integrations in dermal fibroblasts as previously described (90). Dermal fibroblasts were transduced using MOI 10. Both lentiviral supernatants and cells culture medium were supplemented with 8 µg/ml hexadimethrine bromide (Polybrene, Merck). 1 day after transduction, pCCL/PGK-EGFP–treated cells were inspected for green fluorescence as a proxy for successful transduction before the cells were ready for experiments.

Preparation and analysis of samples for flow cytometry

Fibroblasts were washed in PBS prior to detachment by TrypLE Express Enzyme (cat. no. 12563029; Gibco.). Once detached, cells were moved to a 96-well V-shaped plate and pelleted at 400 × g for 5 min. Supernatant was discarded, and cells were washed in 200 µl PBS and subsequently pelleted at 400 × g for 5 min. Supernatant was discarded, and each pellet was resuspended in 50 µl staining solution (0.1 µl live-dead marker, SYTOX Green Dead Cell Stain [#S34860; Invitrogen], 5 µl OSMR Monoclonal Antibody [AN-V2], APC, eBioscience [cat. no. 17-1303-42], and 44.9 µl 1% BSA in PBS) and incubated at RT for 30 min. Included control samples involved single stained cells (only one antibody), dead cells with and without viability stain, and unstained cells. Dead cells were prepared by using permeability buffer (#88-8824-00; Invitrogen) according to manufacturer. After incubation, 200 µl 1% BSA in PBS was added to the cells in staining solution and pelleted at 400 × g for 5 min. Samples/the cells were fixed in 100 µl 2% paraformaldehyde. After fixation, cells were washed with 1% BSA in PBS and resuspended in 100 µl 1% BSA in PBS and kept at 5°C in the dark prior to analysis on a NovoCyte Quanteon flow cytometer (Agilent). Data were analyzed using FlowJo v10.10 (BD biosciences).

PBMCs (5×10^5) were seeded in wells of a 96-well plate. One day after seeding, cells were left untreated or treated for 24 h with 1 µg/ml LPS (from *E. coli* O26:B6, L2654-1MG; Millipore Sigma) and 50 ng/ml IFNγ (Recombinant Human IFN-γ, #300-02; PeproTech). After incubation, cells were washed with PBS, stained for 30 min with LIVE/DEAD Fixable Near-IR Dead Cell Stain (L10119; Invitrogen) in PBS at RT, washed with PBS, and FC blocked for 10 min using Human TruStain FcX (422302; BioLegend) in 1% BSA in PBS. Antibodies for staining of surface markers were directly added to the cells in blocking solution at a final volume of 60 µl. The following antibodies were used: anti-OSMR APC (1:30, clone AN-V2, 17-1303-42; eBioscience), anti-CD19 FITC (1:6, clone HIB19, 555412; BD Biosciences), anti-CD3 Spark Violet 538 (1:30, clone UCHT1, 300484; BioLegend), anti-CD14 Pacific Blue (1:75, clone M5E2, 301815; BioLegend), and anti-CD56 BV786 (1:30, clone RPA-T8, 563823; BD Biosciences) in PBS with 1% BSA. After 30 min of incubation at RT, the cells were washed twice with 1% BSA in PBS, fixed using 2% paraformaldehyde (Sigma-Aldrich), and washed with 1% BSA in PBS. The cells were resuspended in 100 µl 1% BSA in PBS and kept at 5°C in the dark prior to analysis on a Novocyte Quanteon flow cytometer (Agilent). Data were analyzed using FlowJo v10.10 (BD Biosciences).

Statistical analysis

The differences between experimental conditions of groups were analyzed using GraphPad Prism (Version 10) with the type of test indicated in each figure legend. P values ≤0.05 were considered significant: $^*P < 0.05$, $^{**}P < 0.01$, and $^{***}P < 0.001$.

Online supplemental material

Fig. S1 shows patient blood IgE values and HIES score. Fig. S2 shows gating strategies and flow analysis of T cell subsets of Th17, Th9, Th2, and pTFH cell frequencies. Fig. S3 shows Th17 and Th2 subpopulations produce normal levels of IL-17A and IL-4. Fig. S4 shows examination of OSMR surface expression on T and B cells and OSMR variants (>20 CADD score) after deglycosylation. Fig. S5 shows gating strategies for B cell subsets and CSR analyses. Table S1 shows blood values of immunoglobulins, IgG subclasses, hematology, and Th cell subsets from the patient compared to normal ranges from healthy controls. Table S2 shows identification of two monoallelic variants in genes involved in STAT3 signaling.

Data availability

All relevant data that can be shared can be found in supplemental material. Additional data are available from the corresponding author upon reasonable request from health care professionals and within national General Data Protection Regulation rules and regulations.

Acknowledgments

We wish to thank the patient for participating in the study. We also wish to thank Bettina Bundgaard and Lisbeth Jensen for excellent technical assistance. We are grateful to the FACS Core at Aarhus University for expert assistance with flow cytometry experiments.

T.H. Mogensen is supported by the Independent Research Fund Denmark (0134-00006B), the Novo Nordisk Foundation (NNF21OC0067157; NNF20OC0064890), the Lundbeck Foundation (R268-2016-3927), The Innovation Fund Denmark (PASCAL-MID, 8056-00010B), the European Research Council, HORIZON-HLTH-2021-DISEASE-04 program under grant agreement 101057100 (UNDINE), Marie Curie fellowship (DIVIR, 101065126), and the Danish National Research Foundation under the grant agreement DNRF164 (CiViA). S. Andersen received a grant from Frimodt-Heineke Fonden, Læge Sofus Carl Emil Friis og Hustru Olga Doris Friis' Fond and Kong Christian den Tiendes Fond. S.E. Degn received funding from the Independent Research Fund Denmark (Sapere Aude Research Leader grant; 9060-00038) and Aase og Ejnar Danielsens Fond.

Author contributions: Sisse Andersen: conceptualization, data curation, formal analysis, funding acquisition, investigation, methodology, project administration, supervision, validation, visualization, and writing—original draft, review, and editing. Kristian Assing: conceptualization, formal analysis, investigation, methodology, resources, supervision, validation, visualization, and writing—original draft, review, and editing. Julie Jensen: data curation, formal analysis, investigation, methodology, visualization, and writing—review and editing. Line Dahlerup Rasmussen: conceptualization, resources, and writing—review and editing. Christian B. Laursen: conceptualization, data curation, investigation, validation, visualization, and writing—review and editing. Christoffer D. Dellgren: investigation. Daniëla Maria Hinke: formal analysis, investigation, methodology, and visualization. Søren E. Degn: formal analysis, investigation, methodology, resources, and writing—review and editing. Trine H. Mogensen: conceptualization, formal analysis, funding acquisition, investigation, methodology, project administration, resources, supervision, validation, and writing—original draft, review, and editing.

Disclosures: C.B. Laursen reported personal fees from Boehringer Ingelheim, personal fees from GSK, personal fees from Chiesi Pharma, and personal fees from AstraZeneca outside the submitted work. No other disclosures were reported.

Submitted: 15 June 2025
Revised: 21 December 2025
Accepted: 2 February 2026

References

1. Freeman, A.F., and S.M. Holland. 2008. The hyper-IgE syndromes. *Immunol. Allergy Clin. North Am.* 28:277–291, viii. https://doi.org/10.1016/j.iac.2008.01.005
2. Davis, S.D., J. Schaller, and R.J. Wedgwood. 1966. Job's syndrome. Recurrent, "cold", staphylococcal abscesses. *Lancet*. 1:1013–1015. https://doi.org/10.1016/s0140-6736(66)90119-x
3. Buckley, R.H., B.B. Wray, and E.Z. Belmaker. 1972. Extreme hyperimmunoglobulinemia E and undue susceptibility to infection. *Pediatrics*. 49:59–70.
4. Grimbacher, B., S.M. Holland, J.I. Gallin, F. Greenberg, S.C. Hill, H.L. Malech, J.A. Miller, A.C. O'Connell, and J.M. Puck. 1999. Hyper-IgE syndrome with recurrent infections--an autosomal dominant multisystem disorder. *N. Engl. J. Med.* 340:692–702. https://doi.org/10.1056/NEJM199903043400904
5. Chandesris, M.O., I. Melki, A. Natividad, A. Puel, C. Fieschi, L. Yun, C. Thumerelle, E. Oksenhendler, D. Boutboul, C. Thomas, et al. 2012. Autosomal dominant STAT3 deficiency and hyper-IgE syndrome: Molecular, cellular, and clinical features from a French national survey. *Medicine*. 91:e1–e19. https://doi.org/10.1097/MD.0b013e31825f95b9
6. Minegishi, Y., M. Saito, S. Tsuchiya, I. Tsuge, H. Takada, T. Hara, N. Kawamura, T. Ariga, S. Pasic, O. Stojkovic, et al. 2007. Dominant-negative mutations in the DNA-binding domain of STAT3 cause hyper-IgE syndrome. *Nature*. 448:1058–1062. https://doi.org/10.1038/nature06096
7. Holland, S.M., F.R. DeLeo, H.Z. Elloumi, A.P. Hsu, G. Uzel, N. Brodsky, A.F. Freeman, A. Demidowich, J. Davis, M.L. Turner, et al. 2007. STAT3 mutations in the hyper-IgE syndrome. *N. Engl. J. Med.* 357:1608–1619. https://doi.org/10.1056/NEJMoa073687
8. Mogensen, T.H. 2013. STAT3 and the hyper-IgE syndrome: Clinical presentation, genetic origin, pathogenesis, novel findings and remaining uncertainties. *JAKSTAT*. 2:e23435. https://doi.org/10.4161/jkst.23435
9. Tsilifis, C., A.F. Freeman, and A.R. Gennery. 2021. STAT3 hyper-IgE syndrome-an update and unanswered questions. *J. Clin. Immunol.* 41: 864–880. https://doi.org/10.1007/s10875-021-01051-1
10. Philips, R.L., Y. Wang, H. Cheon, Y. Kanno, M. Gadina, V. Sartorelli, C.M. Horvath, J.E. Darnell Jr, G.R. Stark, and J.J. O'Shea. 2022. The JAK-STAT pathway at 30: Much learned, much more to do. *Cell*. 185:3857–3876. https://doi.org/10.1016/j.cell.2022.09.023
11. Larsen, C.S., M. Christiansen, and T.H. Mogensen. 2019. Autosomal dominant hyper-IgE syndrome without significantly elevated IgE. *J. Clin. Immunol.* 39:827–831. https://doi.org/10.1007/s10875-019-00683-8
12. Zhang, Q., B. Boisson, V. Béziat, A. Puel, and J.-L. Casanova. 2018. Human hyper-IgE syndrome: Singular or plural? *Mamm. Genome*. 29:603–617. https://doi.org/10.1007/s00335-018-9767-2
13. Dagoneau, N., D. Scheffer, C. Huber, L.I. Al-Gazali, M. Di Rocco, A. Godard, J. Martinovic, A. Raas-Rothschild, S. Sigaudy, S. Unger, et al. 2004. Null leukemia inhibitory factor receptor (LIFR) mutations in Stuve-Wiedemann/Schwartz-Jampel type 2 syndrome. *Am. J. Hum. Genet.* 74:298–305. https://doi.org/10.1086/381715
14. Mogensen, T.H. 2016. Primary immunodeficiencies with elevated IgE. *Int. Rev. Immunol.* 35:39–56. https://doi.org/10.3109/08830185.2015.1027820
15. Beziat, V., S.J. Tavernier, Y.H. Chen, C.S. Ma, M. Materna, A. Laurence, J. Staal, D. Aschenbrenner, L. Roels, L. Worley, et al. 2020. Dominant-negative mutations in human IL6ST underlie hyper-IgE syndrome. *J. Exp. Med.* 217:e20191804. https://doi.org/10.1084/jem.20191804
16. Ma, C.A., J.R. Stinson, Y. Zhang, J.K. Abbott, M.A. Weinreich, P.J. Hauk, P.R. Reynolds, J.J. Lyons, C.G. Nelson, E. Ruffo, et al. 2017. Germline hypomorphic CARD11 mutations in severe atopic disease. *Nat. Genet.* 49: 1192–1201. https://doi.org/10.1038/ng.3898
17. Sharma, M., D. Leung, M. Momenilandi, L.C.W. Jones, L. Pacillo, A.E. James, J.R. Murrell, S. Delafontaine, J. Maimaris, M. Vaseghi-Shanjani, et al. 2023. Human germline heterozygous gain-of-function STAT6 variants cause severe allergic disease. *J. Exp. Med.* 220:e20221755. https://doi.org/10.1084/jem.20221755
18. Lyons, J.J., Y. Liu, C.A. Ma, X. Yu, M.P. O'Connell, M.G. Lawrence, Y. Zhang, K. Karpe, M. Zhao, A.M. Siegel, et al. 2017. ERBIN deficiency links STAT3 and TGF-beta pathway defects with atopy in humans. *J. Exp. Med.* 214:669–680. https://doi.org/10.1084/jem.20161435
19. Droghini, H.R., J.P. Abonia, M.H. Collins, J.D. Milner, J.J. Lyons, A.F. Freeman, V.A. Mukkada, K.A. Risma, M.E. Rothenberg, and J.T. Schwartz. 2022. Targeted IL-4Ralpha blockade ameliorates refractory allergic eosinophilic inflammation in a patient with dysregulated TGF-beta signaling due to ERBIN deficiency. *J. Allergy Clin. Immunol. Pract.* 10: 1903–1906. https://doi.org/10.1016/j.jaip.2022.01.012
20. Zhang, Q., J.C. Davis, I.T. Lamborn, A.F. Freeman, H. Jing, A.J. Favreau, H.F. Matthews, J. Davis, M.L. Turner, G. Uzel, et al. 2009. Combined immunodeficiency associated with DOCK8 mutations. *N. Engl. J. Med.* 361:2046–2055. https://doi.org/10.1056/NEJMoa0905506
21. Frey-Jakobs, S., J.M. Hartberger, M. Fliegauf, C. Bossen, M.L. Wehmeyer, J.C. Neubauer, A. Bulashevska, M. Proietti, P. Fröbel, C. Nöltner, et al. 2018. ZNF341 controls STAT3 expression and thereby immunocompetence. *Sci. Immunol.* 3:eaat4941. https://doi.org/10.1126/sciimmunol.aat4941
22. Beziat, V., J. Li, J.X. Lin, C.S. Ma, P. Li, A. Bousfiha, I. Pellier, S. Zoghi, S. Baris, S. Keles, et al. 2018. A recessive form of hyper-IgE syndrome by disruption of ZNF341-dependent STAT3 transcription and activity. *Sci. Immunol.* 3:eaat4956. https://doi.org/10.1126/sciimmunol.aat4956
23. Sassi, A., S. Lazaroski, G. Wu, S.M. Haslam, M. Fliegauf, F. Mellouli, T. Patiroglu, E. Unal, M.A. Ozdemir, Z. Jouhadi Z, et al. 2014. Hypomorphic homozygous mutations in phosphoglucomutase 3 (PGM3) impair immunity and increase serum IgE levels. J. Allergy Clin. Immunol. 133:1410–1419, 1419 e1–13. https://doi.org/10.1016/j.jaci.2014.02.025
24. Zhang, Y., X. Yu, M. Ichikawa, J.J. Lyons, S. Datta, I.T. Lamborn, H. Jing, E.S. Kim, M. Biancalana, L.A. Wolfe, et al. 2014. Autosomal recessive phosphoglucomutase 3 (PGM3) mutations link glycosylation defects to atopy, immune deficiency, autoimmunity, and neurocognitive impairment. J. Allergy Clin. Immunol. 133:1400–1409, 1409 e1–5. https://doi.org/10.1016/j.jaci.2014.02.013
25. Ben-Ali, M., L. Ben-Khemis, N. Mekki, R. Yaakoubi, R. Ouni, C. Benabdessalem, I. Ben-Mustapha, and M.-R. Barbouche. 2019. Defective glycosylation leads to defective gp130-dependent STAT3 signaling in PGM3-deficient patients. *J. Allergy Clin. Immunol.* 143:1638–1640.e2. https://doi.org/10.1016/j.jaci.2018.12.987
26. Frede, N., J. Rojas-Restrepo, A. Caballero Garcia de Oteyza, M. Buchta, K. Hübscher, L. Gámez-Díaz, M. Proietti, S. Saghafi, Z. Chavoshzadeh,

P. Soler-Palacin, et al. 2021. Genetic analysis of a cohort of 275 patients with hyper-IgE syndromes and/or chronic mucocutaneous candidiasis. *J. Clin. Immunol.* 41:1804–1838. https://doi.org/10.1007/s10875-021-01086-4

27. Schwerd, T., S.R.F. Twigg, D. Aschenbrenner, S. Manrique, K.A. Miller, I.B. Taylor, M. Capitani, S.J. McGowan, E. Sweeney, A. Weber, et al. 2017. A biallelic mutation in IL6ST encoding the GP130 co-receptor causes immunodeficiency and craniosynostosis. *J. Exp. Med.* 214:2547–2562. https://doi.org/10.1084/jem.20161810
28. Spencer, S., S. Köstel Bal, W. Egner, H. Lango Allen, S.I. Raza, C.A. Ma, M. Gürel, Y. Zhang, G. Sun, R.A. Sabroe, et al. 2019. Loss of the interleukin-6 receptor causes immunodeficiency, atopy, and abnormal inflammatory responses. *J. Exp. Med.* 216:1986–1998. https://doi.org/10.1084/jem.20190344
29. Kane, A., E.K. Deenick, C.S. Ma, M.C. Cook, G. Uzel, and S.G. Tangye. 2014. STAT3 is a central regulator of lymphocyte differentiation and function. *Curr. Opin. Immunol.* 28:49–57. https://doi.org/10.1016/j.coi.2014.01.015
30. Stritesky, G.L., R. Muthukrishnan, S. Sehra, R. Goswami, D. Pham, J. Travers, E.T. Nguyen, D.E. Levy, and M.H. Kaplan. 2011. The transcription factor STAT3 is required for T helper 2 cell development. *Immunity*. 34:39–49. https://doi.org/10.1016/j.immuni.2010.12.013
31. Vempati, R.K. 2023. Cloning, expression, purification, and immunoblotting analysis of recombinant type III fibronectin domains of human oncostatin M receptor. *Mol. Biol. Rep.* 50:4735–4741. https://doi.org/10.1007/s11033-023-08366-9
32. Dillon, S.R., C. Sprecher, A. Hammond, J. Bilsborough, M. Rosenfeld-Franklin, S.R. Presnell, H.S. Haugen, M. Maurer, B. Harder, J. Johnston, et al. 2004. Interleukin 31, a cytokine produced by activated T cells, induces dermatitis in mice. *Nat. Immunol.* 5:752–760. https://doi.org/10.1038/ni1084
33. Lantieri, F., and T. Bachetti. 2022. OSM/OSMR and interleukin 6 family cytokines in physiological and pathological condition. *Int. J. Mol. Sci.* 23:11096. https://doi.org/10.3390/ijms231911096
34. Zhang, Q., P. Putheti, Q. Zhou, Q. Liu, and W. Gao. 2008. Structures and biological functions of IL-31 and IL-31 receptors. *Cytokine Growth Factor Rev.* 19:347–356. https://doi.org/10.1016/j.cytogfr.2008.08.003
35. Hermanns, H.M. 2015. Oncostatin M and interleukin-31: Cytokines, receptors, signal transduction and physiology. *Cytokine Growth Factor Rev.* 26:545–558. https://doi.org/10.1016/j.cytogfr.2015.07.006
36. Lutticken, C., U.M. Wegenka, J. Yuan, J. Buschmann, C. Schindler, A. Ziemiecki, A.G. Harpur, A.F. Wilks, K. Yasukawa, T. Taga, et al. 1994. Association of transcription factor APRF and protein kinase Jak1 with the interleukin-6 signal transducer gp130. *Science*. 263:89–92. https://doi.org/10.1126/science.8272872
37. Hunter, C.A., and S.A. Jones. 2015. IL-6 as a keystone cytokine in health and disease. *Nat. Immunol.* 16:448–457. https://doi.org/10.1038/ni.3153
38. Murakami, M., D. Kamimura, and T. Hirano. 2019. Pleiotropy and specificity: Insights from the interleukin 6 family of cytokines. *Immunity*. 50:812–831. https://doi.org/10.1016/j.immuni.2019.03.027
39. West, N.R., B.M.J. Owens, and A.N. Hegazy. 2018. The oncostatin M-stromal cell axis in health and disease. *Scand. J. Immunol.* 88:e12694. https://doi.org/10.1111/sji.12694
40. Garbers, C., S. Heink, T. Korn, and S. Rose-John. 2018. Interleukin-6: Designing specific therapeutics for a complex cytokine. *Nat. Rev. Drug Discov.* 17:395–412. https://doi.org/10.1038/nrd.2018.45
41. Chollangi, S., T. Mather, K.K. Rodgers, and J.D. Ash. 2012. A unique loop structure in oncostatin M determines binding affinity toward oncostatin M receptor and leukemia inhibitory factor receptor. *J. Biol. Chem.* 287:32848–32859. https://doi.org/10.1074/jbc.M112.387324
42. Nicola, N.A., and J.J. Babon. 2015. Leukemia inhibitory factor (LIF). *Cytokine Growth Factor Rev.* 26:533–544. https://doi.org/10.1016/j.cytogfr.2015.07.001
43. Lai, T., D. Wu, W. Li, M. Chen, Z. Yi, D. Huang, Z. Jing, Y. Lü, Q. Lv, D. Li, and B. Wu. 2016. Interleukin-31 expression and relation to disease severity in human asthma. *Sci. Rep.* 6:22835. https://doi.org/10.1038/srep22835
44. Bagci, I.S., and T. Ruzicka. 2018. IL-31: A new key player in dermatology and beyond. *J. Allergy Clin. Immunol.* 141:858–866. https://doi.org/10.1016/j.jaci.2017.10.045
45. Tanaka, M., Y. Hirabayashi, T. Sekiguchi, T. Inoue, M. Katsuki, and A. Miyajima. 2003. Targeted disruption of oncostatin M receptor results in altered hematopoiesis. *Blood*. 102:3154–3162. https://doi.org/10.1182/blood-2003-02-0367
46. Tanaka, A., J.E. Lai-Cheong, P.C. van den Akker, N. Nagy, G. Millington, G.F.H. Diercks, P.C. van Voorst Vader, S.E. Clements, N. Almaani, T. Techanukul, et al. 2010. The molecular skin pathology of familial primary localized cutaneous amyloidosis. *Exp. Dermatol.* 19:416–423. https://doi.org/10.1111/j.1600-0625.2010.01083.x
47. Adams, R., C. Colmont, A. Mukhtar, H. Morgan, and G.K. Patel. 2020. A novel oncostatin M/interleukin-31 receptor mutation in familial primary localized cutaneous amyloidosis. *Clin. Exp. Dermatol.* 45:254–256. https://doi.org/10.1111/ced.14059
48. Garrigue, A., L. Kermasson, S. Susini, I. Fert, C.B. Mahony, H. Sadek, S. Luce, M. Chouteau, M. Cavazzana, E. Six, et al. 2025. Human oncostatin M deficiency underlies an inherited severe bone marrow failure syndrome. *J. Clin. Invest.* 135:e180981. https://doi.org/10.1172/JCI180981
49. Tangye, S.G., W. Al-Herz, A. Bousfiha, T. Chatila, C. Cunningham-Rundles, A. Etzioni, J.L. Franco, S.M. Holland, C. Klein, T. Morio, et al. 2020. Human inborn errors of immunity: 2019 Update on the classification from the international union of immunological Societies expert committee. *J. Clin. Immunol.* 40:24–64. https://doi.org/10.1007/s10875-019-00737-x
50. Bousfiha, A., A. Moundir, S.G. Tangye, C. Picard, L. Jeddane, W. Al-Herz, C.C. Rundles, J.L. Franco, S.M. Holland, C. Klein, et al. 2022. The 2022 update of IUIS phenotypical classification for human inborn errors of immunity. *J. Clin. Immunol.* 42:1508–1520. https://doi.org/10.1007/s10875-022-01352-z
51. Arita, K., A.P. South, G. Hans-Filho, T.H. Sakuma, J. Lai-Cheong, S. Clements, M. Odashiro, D.N. Odashiro, G. Hans-Neto, N.R. Hans, et al. 2008. Oncostatin M receptor-beta mutations underlie familial primary localized cutaneous amyloidosis. *Am. J. Hum. Genet.* 82:73–80. https://doi.org/10.1016/j.ajhg.2007.09.002
52. Bio, E. 2025. ICE CRISPR Analysis v.3.0. Dec. 19, 2025.
53. Jawa, R.S., S. Chattopadhyay, E. Tracy, Y. Wang, K. Huntoon, M.T. Dayton, and H. Baumann. 2008. Regulated expression of the IL-31 receptor in bronchial and alveolar epithelial cells, pulmonary fibroblasts, and pulmonary macrophages. *J. Interferon Cytokine Res.* 28:207–219. https://doi.org/10.1089/jir.2007.0057
54. Richards, C.D. 2013. The enigmatic cytokine oncostatin m and roles in disease. *ISRN Inflamm.* 2013:512103. https://doi.org/10.1155/2013/512103
55. Digre, A., and C. Lindskog. 2023. The human protein atlas-Integrated omics for single cell mapping of the human proteome. *Protein Sci.* 32:e4562. https://doi.org/10.1002/pro.4562
56. Karlsson, M., C. Zhang, L. Méar, W. Zhong, A. Digre, B. Katona, E. Sjöstedt, L. Butler, J. Odeberg, P. Dusart, et al. 2021. A single-cell type transcriptomics map of human tissues. *Sci. Adv.* 7:eabh2169. https://doi.org/10.1126/sciadv.abh2169
57. Speckmann, C., A. Enders, C. Woellner, D. Thiel, A. Rensing-Ehl, M. Schlesier, J. Rohr, T. Jakob, E. Oswald, M.V. Kopp, et al. 2008. Reduced memory B cells in patients with hyper IgE syndrome. *Clin. Immunol.* 129:448–454. https://doi.org/10.1016/j.clim.2008.08.002
58. Horst, A., N. Hunzelmann, S. Arce, M. Herber, R.A. Manz, A. Radbruch, R. Nischt, J. Schmitz, and M. Assenmacher. 2002. Detection and characterization of plasma cells in peripheral blood: Correlation of IgE+ plasma cell frequency with IgE serum titre. *Clin. Exp. Immunol.* 130:370–378. https://doi.org/10.1046/j.1365-2249.2002.02025.x
59. Rovsing, A.B., K. Green, L. Jensen, I.H. Nielsen, J.G. Mikkelsen, and S.E. Degn. 2025. Multiparametric optimization of human primary B-cell cultures using design of experiments. *Scand. J. Immunol.* 102:e70043. https://doi.org/10.1111/sji.70043
60. Ma, C.S., G.Y.J. Chew, N. Simpson, A. Priyadarshi, M. Wong, B. Grimbacher, D.A. Fulcher, S.G. Tangye, and M.C. Cook. 2008. Deficiency of Th17 cells in hyper IgE syndrome due to mutations in STAT3. *J. Exp. Med.* 205:1551–1557. https://doi.org/10.1084/jem.20080218
61. Schwerd, T., F. Krause, S.R.F. Twigg, D. Aschenbrenner, Y.-H. Chen, U. Borgmeyer, M. Müller, S. Manrique, N. Schumacher, S.A. Wall, et al. 2020. A variant in IL6ST with a selective IL-11 signaling defect in human and mouse. *Bone Res.* 8:24. https://doi.org/10.1038/s41413-020-0098-z
62. Guihard, P., Y. Danger, B. Brounais, E. David, R. Brion, J. Delecrin, C.D. Richards, S. Chevalier, F. Rédini, D. Heymann, et al. 2012. Induction of osteogenesis in mesenchymal stem cells by activated monocytes/macrophages depends on oncostatin M signaling. *Stem Cells*. 30:762–772. https://doi.org/10.1002/stem.1040
63. Persson, E., P.P.C. Souza, T. Floriano-Marcelino, H.H. Conaway, P. Henning, and U.H. Lerner. 2019. Activation of Shc1 allows oncostatin M to induce RANKL and osteoclast formation more effectively than

leukemia inhibitory factor. *Front. Immunol.* 10:1164. https://doi.org/10.3389/fimmu.2019.01164

64. Hergovits, S., C. Mais, C. Haan, A.P. Costa-Pereira, and H.M. Hermanns. 2017. Oncostatin M induces RIG-I and MDA5 expression and enhances the double-stranded RNA response in fibroblasts. *J. Cell Mol. Med.* 21: 3087–3099. https://doi.org/10.1111/jcmm.13221
65. Le Goff, B., S. Singbrant, B.A. Tonkin, T.J. Martin, E. Romas, N.A. Sims, and N.C. Walsh. 2014. Oncostatin M acting via OSMR, augments the actions of IL-1 and TNF in synovial fibroblasts. *Cytokine*. 68:101–109. https://doi.org/10.1016/j.cyto.2014.04.001
66. Wong, Z.Y., E. Nee, M. Coles, and C.D. Buckley. 2023. Why does understanding the biology of fibroblasts in immunity really matter? *PLoS Biol.* 21:e3001954. https://doi.org/10.1371/journal.pbio.3001954
67. Cavagnero, K.J., and R.L. Gallo. 2022. Essential immune functions of fibroblasts in innate host defense. *Front. Immunol.* 13:1058862. https://doi.org/10.3389/fimmu.2022.1058862
68. Jeong, E.J., I.Y. Lee, J.-S. Choi, I.S. Cheon, G. Kang, and J. Choe. 2004. Fibroblasts enhance the in vitro survival of human memory and naive B cells by maintaining intracellular levels of glutathione. *Mol. Cells*. 17: 430–437. https://doi.org/10.1016/S1016-8478(23)25239-5
69. Lianos, K.S.A., and A.L. Fletcher. 2021. Fibroblasts: The B’s knees of follicular lymphoma. *Immunity*. 54:1628–1630. https://doi.org/10.1016/j.immuni.2021.07.016
70. Lutge, M., N.B. Pikor, and B. Ludewig. 2021. Differentiation and activation of fibroblastic reticular cells. *Immunol. Rev.* 302:32–46. https://doi.org/10.1111/imr.12981
71. King, I.L., and M. Mohrs. 2009. IL-4-producing CD4+ T cells in reactive lymph nodes during helminth infection are T follicular helper cells. *J. Exp. Med.* 206:1001–1007. https://doi.org/10.1084/jem.20090313
72. Reid, J., S. Zamuner, K. Edwards, S.-A. Rumley, K. Nevin, M. Feeney, C. Zecchin, D. Fernando, and N. Wisniacki. 2018. In vivo affinity and target engagement in skin and blood in a first-time-in-human study of an anti-oncostatin M monoclonal antibody. *Br. J. Clin. Pharmacol.* 84:2280–2291. https://doi.org/10.1111/bcp.13669
73. Minehata, K., M. Takeuchi, Y. Hirabayashi, T. Inoue, P.J. Donovan, M. Tanaka, and A. Miyajima. 2006. Oncostatin m maintains the hematopoietic microenvironment and retains hematopoietic progenitors in the bone marrow. *Int. J. Hematol.* 84:319–327. https://doi.org/10.1532/IJH97.06090
74. Romeo Bertola, D., R.S. Honjo, and W.A. Baratela. 2016. Stuve-Wiedemann syndrome: Update on clinical and genetic aspects. *Mol. Syndromol.* 7:12–18. https://doi.org/10.1159/000444729
75. Puel, A., and J.L. Casanova. 2019. The nature of human IL-6. *J. Exp. Med.* 216:1969–1971. https://doi.org/10.1084/jem.20191002
76. Arai, I., and S. Saito. 2023. Interleukin-31 receptor A expression in the dorsal root ganglion of mice with atopic dermatitis. *Int. J. Mol. Sci.* 24: 1047. https://doi.org/10.3390/ijms24021047
77. Perrigoue, J.G., J. Li, C. Zaph, M. Goldschmidt, P. Scott, F.J. de Sauvage, E.J. Pearce, N. Ghilardi, and D. Artis. 2007. IL-31-IL-31R interactions negatively regulate type 2 inflammation in the lung. *J. Exp. Med.* 204: 481–487. https://doi.org/10.1084/jem.20061791
78. Huang, J., H. Yue, T. Jiang, J. Gao, Y. Shi, B. Shi, X. Wu, and X. Gou. 2019. IL-31 plays dual roles in lung inflammation in an OVA-induced murine asthma model. *Biol. Open.* 8:bio036244. https://doi.org/10.1242/bio.036244
79. Yombo, D.J.K., V. Odayar, N. Gupta, A.G. Jegga, and S.K. Madala. 2021. The protective effects of IL-31RA deficiency during bleomycin-induced pulmonary fibrosis. *Front. Immunol.* 12:645717. https://doi.org/10.3389/fimmu.2021.645717
80. Li, H. 2013. Aligning sequence reads, clone sequences and assembly contigs with BWA-MEM. https://arxiv.org/abs/1303.3997 (Preprint posted May 26, 2013)
81. Richards, S., N. Aziz, S. Bale, D. Bick, S. Das, J. Gastier-Foster, W.W. Grody, M. Hegde, E. Lyon, E. Spector, et al. 2015. Standards and guidelines for the interpretation of sequence variants: A joint consensus recommendation of the American college of medical genetics and genomics and the association for molecular pathology. *Genet. Med.* 17:405–424. https://doi.org/10.1038/gim.2015.30
82. Rentzsch, P., D. Witten, G.M. Cooper, J. Shendure, and M. Kircher. 2019. CADD: Predicting the deleteriousness of variants throughout the human genome. *Nucleic Acids Res.* 47:D886–D894. https://doi.org/10.1093/nar/gky1016
83. Zhang, P., B. Bigio, F. Rapaport, S.-Y. Zhang, J.-L. Casanova, L. Abel, B. Boisson, and Y. Itan. 2018. PopViz: A webserver for visualizing minor allele frequencies and damage prediction scores of human genetic variations. *Bioinformatics*. 34:4307–4309. https://doi.org/10.1093/bioinformatics/bty536
84. Itan, Y., L. Shang, B. Boisson, E. Patin, A. Bolze, M. Moncada-Vélez, E. Scott, M.J. Ciancanelli, F.G. Lafaille, J.G. Markle, et al. 2015. The human gene damage index as a gene-level approach to prioritizing exome variants. *Proc. Natl. Acad. Sci. USA*. 112:13615–13620. https://doi.org/10.1073/pnas.1518646112
85. Poli, Maria, S, I. Aksentijevich, A.A. Bousfiha, C. Cunningham-Rundles, S. Hambleton, C. Klein, T. Morio, C. Picard, A. Puel, N. Rezaei, et al. 2025. Human inborn errors of immunity: 2024 update on the classification from the International Union of Immunological Societies Expert Committee. *J. Hum. Immun.* 1:e20250003. https://doi.org/10.70962/jhi.20250003
86. Keles, S., L.M. Charbonnier, V. Kabaleeswaran, I. Reisli, F. Genel, N. Gulez, W. Al-Herz, N. Ramesh, A. Perez-Atayde, N.E. Karaca, et al. 2016. Dedicator of cytokinesis 8 regulates signal transducer and activator of transcription 3 activation and promotes T(H)17 cell differentiation. *J. Allergy Clin. Immunol.* 138:1384–1394.e2. https://doi.org/10.1016/j.jaci.2016.04.023
87. Levy, R., S. Okada, V. Béziat, K. Moriya, C. Liu, L.Y. Chai, M. Migaud, F. Hauck, A. Al Ali, C. Cyrus, et al. 2016. Genetic, immunological, and clinical features of patients with bacterial and fungal infections due to inherited IL-17RA deficiency. *Proc. Natl. Acad. Sci. USA*. 113:E8277–E8285. https://doi.org/10.1073/pnas.1618300114
88. Livak, K.J., and T.D. Schmittgen. 2001. Analysis of relative gene expression data using real-time quantitative PCR and the 2(-Delta Delta C(T)) method. *Methods*. 25:402–408. https://doi.org/10.1006/meth.2001.1262
89. Hollensen, A.K., R. Thomsen, R.O. Bak, C.C. Petersen, E.R. Ermegaard, L. Aagaard, C.K. Damgaard, and J.G. Mikkelsen. 2017. Improved microRNA suppression by WPRE-linked tough decoy microRNA sponges. *RNA*. 23: 1247–1258. https://doi.org/10.1261/rna.061192.117
90. Bak, R.O., A.K. Hollensen, M.N. Primo, C.D. Sørensen, and J.G. Mikkelsen. 2013. Potent microRNA suppression by RNA pol II-transcribed ‘tough decoy’ inhibitors. *RNA*. 19:280–293. https://doi.org/10.1261/rna.034850.112

Supplemental material

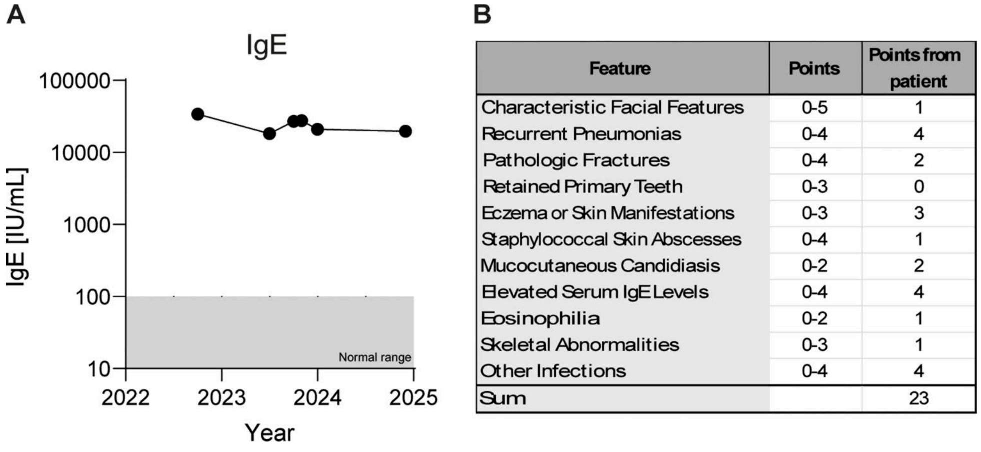

Feature	Points	Points from patient
Characteristic Facial Features	0-5	1
Recurrent Pneumonias	0-4	4
Pathologic Fractures	0-4	2
Retained Primary Teeth	0-3	0
Eczema or Skin Manifestations	0-3	3
Staphylococcal Skin Abscesses	0-4	1
Mucocutaneous Candidiasis	0-2	2
Elevated Serum IgE Levels	0-4	4
Eosinophilia	0-2	1
Skeletal Abnormalities	0-3	1
Other Infections	0-4	4
Sum		23

Figure S1. **Patient blood IgE values and HIES score. (A)** Patient IgE levels in the blood over time since 2022. Grey area indicates the normal range of IgE in blood of healthy controls. **(B)** HIES score of the patient. Each HIES characteristic feature of the patient was evaluated, and points were given been given and calculated accordingly.

https://doi.org/10.70962/jhi.20250119

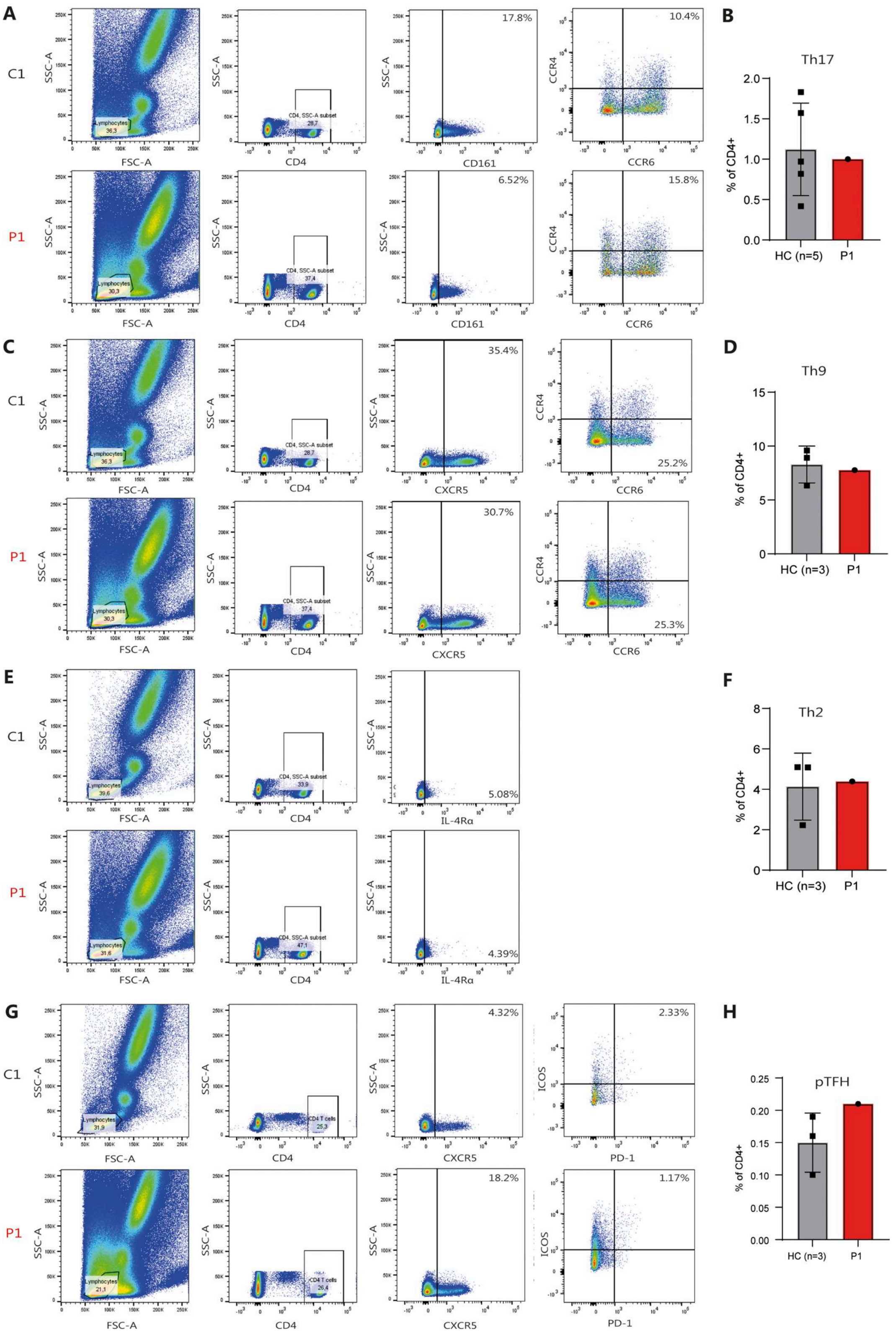

Figure S2. **Gating strategies and flow analysis of T cell subsets of Th17, Th9, Th2, and pTFH cell frequencies. (A)** Gating strategy for Th17 cells, classified as CD4$^+$CD161$^+$ CCR4$^+$CCR6$^+$. The first row shows representative flow plots for five HCs, and the second row shows flow plots for P1. **(B)** Th17 frequencies of CD4$^+$. **(C)** Gating strategy for Th9 cells, classified as CD4$^+$ CXCR3 (indicated as CXCR5 in dot plot)$^+$ CCR4$^-$ CCR6$^+$. The first row shows representative flow plots for three HCs, and the second row shows flow plots for P1. Duplicate of data shown in A, rows 1 and 2. **(D)** Th9 frequencies of CD4$^+$. **(E)** Gating strategy for Th2 cells, classified as CD4$^+$ CD124 (IL-4Ra, indicated as CCR4 in dot plot). The first row shows representative flow plots for three HCs, and the second row shows flow plots for P1. **(F)** Th2 frequencies of CD4$^+$. **(G)** Gating strategy for pTFH cells classified as CD4 (APC)$^+$ CXCR5 (Per-CP)$^+$ ICOS (BV421)$^+$ PD-1$^+$ (PE) in dot plot. **(H)** pTFH cell frequencies of CD4$^+$. HC, healthy control.

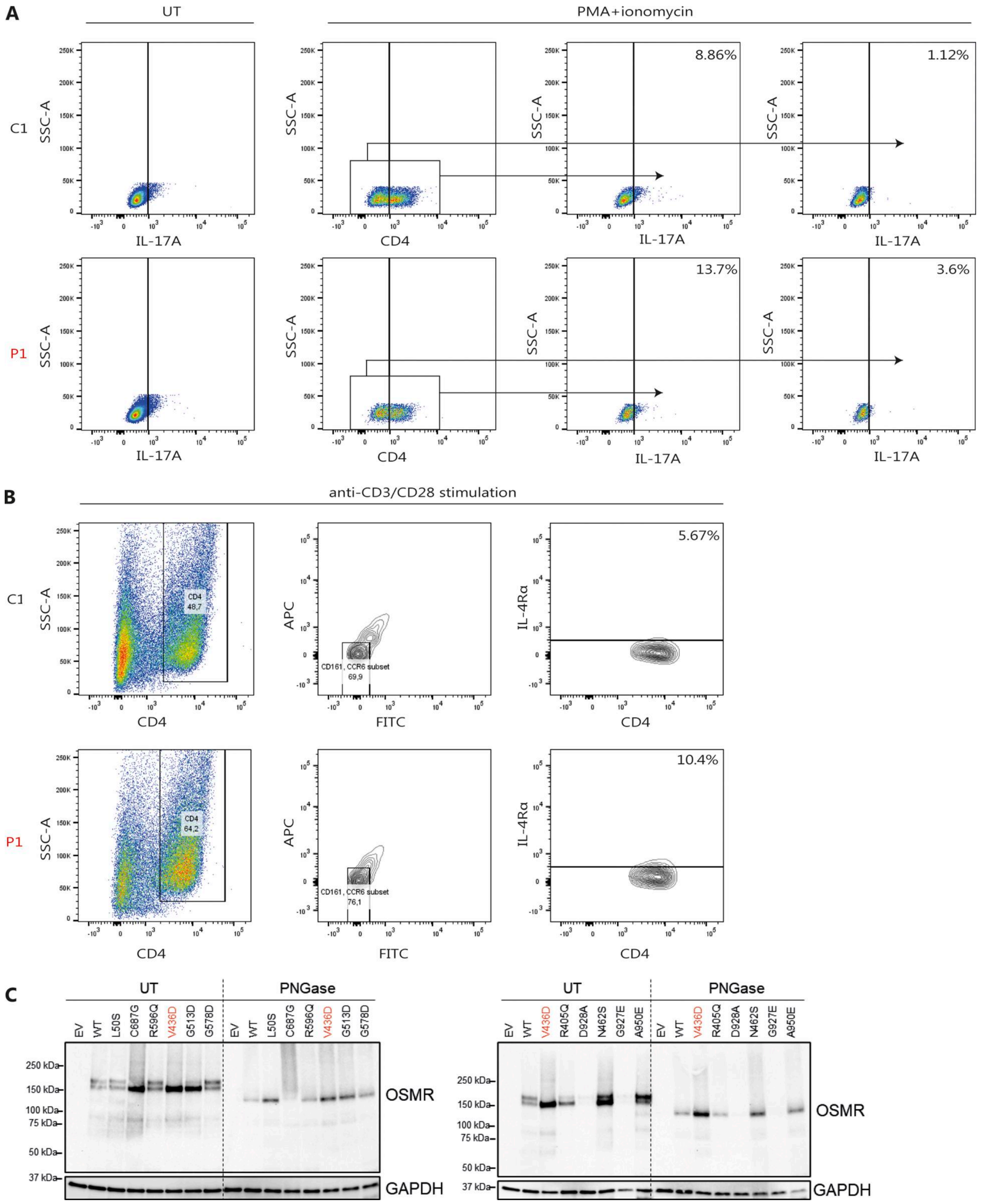

Figure S3. **Patient Th17 and Th2 subpopulations and IL-17A and IL-4 production and predicted deleterious (CADD score >20) *OSMR* variants, including the patient *OSMR* variant, after deglycosylation treatment. (A)** Representative flow plots of CD4$^+$ IL-17A$^+$ T cells from two healthy controls (HCs) (top row) and P1 (bottom row) either untreated (UT; left panels) or treated with PMA and ionomycin for 4 h (right panels). **(B)** Representative flow plots of the frequency of CD4$^+$ IL-4Ra-positive T cells from two HCs and P1 treated with anti-CD3/CD28 for 5 days. Left dot plot: anti-CD3/CD28-stimulated CD4 (PerCP-conjugated) T cells displayed SSC characteristics consistent with CD4 T cell blasts. Central dot plot: to compensate for autofluorescent CD4 T blast cells, the APC and FITC channel (no antibodies added) were used to define non-autofluorescent CD4 T cells. Right dot plot: from the non-autofluorescent CD4 T cell gate, the fraction of IL-4Ra$^+$ (PE-conjugated) CD4 T cells was defined (IL-4Ra cutoff having been priorly defined as IL-4Ra negativity in the FITC channel along the y axis, not shown). **(C)** Untreated (UT) and N-deglycosylase PNGase-treated cell lysates of HEK293 cells transfected with empty vector (EV), *OSMR* WT, and predicted deleterious *OSMR* variants. The *OSMR* variant harbored by P1 is marked in red. Source data are available for this figure: SourceData FS3.

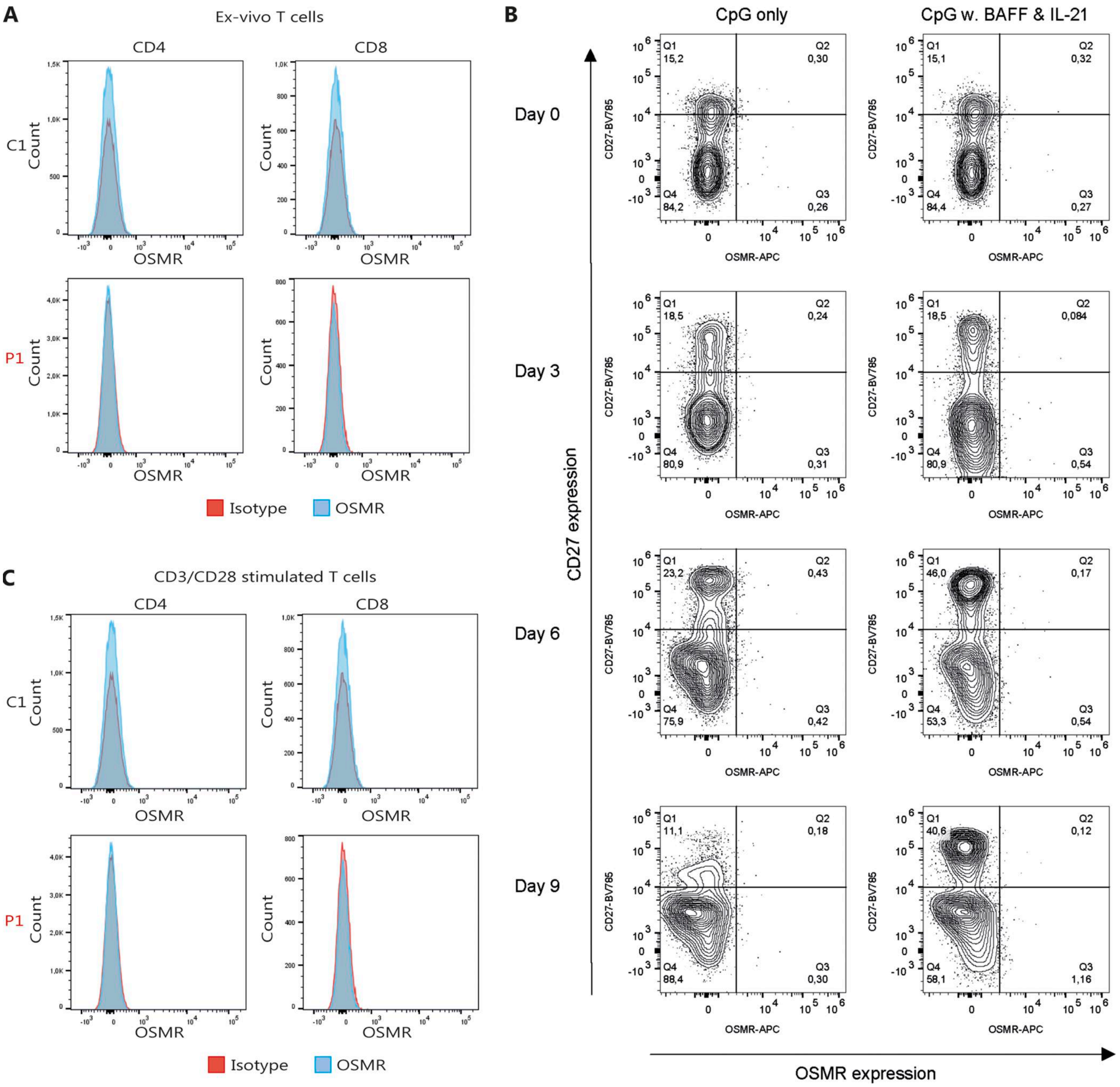

Figure S4. **Examination of OSMR surface expression on T and B cells. (A)** Representative flow plots of OSMR (APC) expression of ex vivo–unstimulated CD4⁺ CD8⁺ T cells from one of two healthy controls (HCs) and one P1. **(B)** Histograms of 5 days anti-CD3/CD28-stimulated CD4⁺ CD8⁺ T cells from P1 showing the OSMR-APC channel. **(C)** PBMCs (500,000 cells) from HCs were incubated with CpG (ODN 2006, 2 µg/ml) alone (left panel) or CpG (2 µg/ml), BAFF (10 ng/ml), and IL-21 (10 ng/ml) (right panel) in the BCM for various days as shown. The vertical axis of the flow plots shows the progression of CD27, and the horizontal axis of the flow plots shows the OSMR expression.

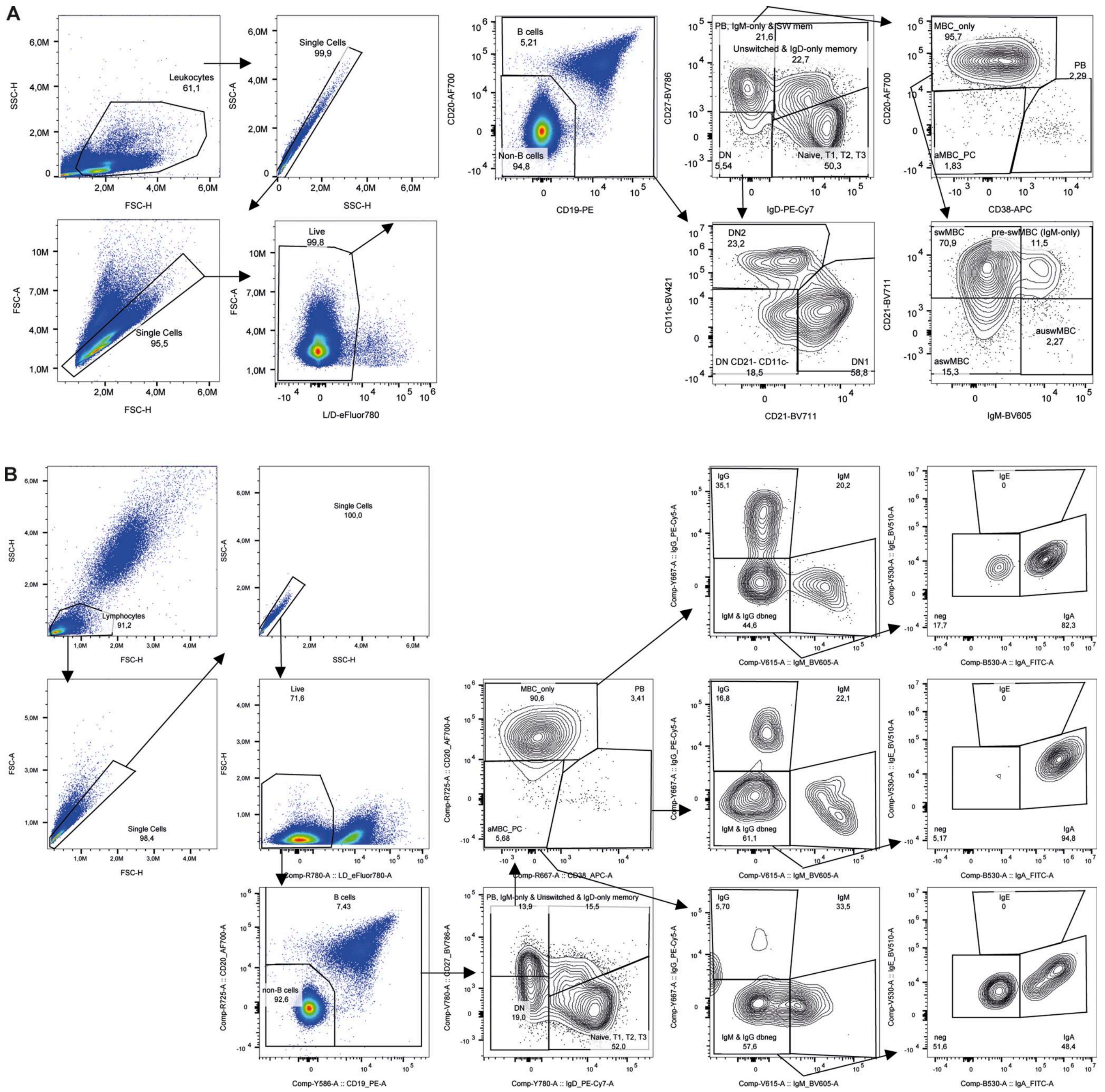

Figure S5. **Gating strategies for B cell subsets and CSR analyses. (A)** Gating strategy for B cell subset analyses of PBMCs. (Data shown in row 1, columns 4 and 5 are identical to data shown in Fig. 5A, rows 1 and 2, column 1.) **(B)** Gating strategy for CSR analyses from full blood. aMBC_PC, aMBC/plasma cell; (a)swMBC, (atypical) switched memory B cell; auswMBC, atypical unswitched memory B cell; DN, double-negative B cell subset; dbneg, double-negative for markers in respective bivariate plot; MBC_only, conventional memory B cell; SWmem, switched memory; T1, T2, T3, transitional 1, 2, 3 subsets.

Provided online are Table S1 and Table S2. Table S1 shows blood values of immunoglobulins, IgG subclasses, hematology, and T helper cell subsets from the patient compared to normal ranges from healthy controls. Table S2 shows identification of two monoallelic variants in genes involved in STAT3 signaling.